CYCLIC TEST ON A PRECAST REINFORCED CONCRETE COLUMN-TO-FOUNDATION GROUTED DUCT CONNECTION

Nerio TULLINI[a], Fabio MINGHINI[b]

Engineering Department, University of Ferrara, Via Saragat 1, Ferrara, Italy

[a] Corresponding author. E-mail: nerio.tullini@unife.it; Phone: +39 (0) 532 974936

[b] E-mail: fabio.minghini@unife.it

ABSTRACT

A full-scale specimen of a column-to-foundation grouted duct connection suited for buildings and industrial structures is tested in cyclic bending combined with axial compression. The positioning of the steel ducts along the sides of the column cross-section allows for using traditional reinforcement cages for the column, with longitudinal bars at both mid-side and corners of the cross-section. Splice length and amount of transverse reinforcement along the splice are defined based on Eurocode 2 provisions for laps of reinforcing bars.

A total of 19 loading cycles are carried out, achieving a drift of 5.3% in correspondence of a degradation of 15% of the peak resistance. The shear slip measured at the column-foundation interface results to be smaller than 5% of the deflection. Conversely, to predict accurately the test results, the slip of the projecting bars within their ducts cannot be neglected. It is proposed to take account of this slip by introducing an apparent strain. For the tested specimen, the apparent strain turns out to be equal to the yield strain of the reinforcement. A comparison with a monotonic bending test, previously conducted on the same connection, shows a strongly smaller deformability when the loading protocol is cyclic.

Hysteretic energy and drift ductility for the proposed connection are close to those concerning a cast-in-place specimen of comparable capacity, which was described in a recent paper.

The test results show an over-strength of 1.4 and a gain in ductility of 1.8 compared with the design values of bending resistance and curvature ductility computed for the cross-section at the column-foundation interface.

Keywords: Precast concrete column; Column-to-foundation connection; Grouted duct connection; Cyclic test; Ductility; Bar slip

1. INTRODUCTION

In precast Reinforced Concrete (RC) construction, the connection behavior considerably influences the overall structural response (Elliot 2017), particularly of precast structures subjected to earthquake loading. In fact, when they are inadequate, catastrophic failure may occur, as was testified by past earthquakes (Yanev 1989; Sezen and Whittaker 2006; Toniolo and Colombo 2012; Belleri et al. 2015; Minghini et al. 2016; Savoia et al. 2017; Buratti et al. 2017) and demonstrated by recent numerical investigations (Bovo and Savoia 2018; Demartino et al. 2018). In view of future earthquakes, the scientific community is then becoming more sensitive to the need of innovative connections with suitable strength and ductility (Negro and Toniolo 2012).

Grouted joints are gaining increasing importance for earthquake resistant structures made of precast RC elements. They can be designed to develop strength and ductility comparable with those of cast-in-place connections and offer the advantage of a quick assembly. Among the connection types based on splicing of the longitudinal reinforcement, two main categories can be identified: (1) connections using bar couplers and (2) grouted duct connections.

The connections using bar couplers (Hua et al. 2014; Yuan et al. 2017; Liu et al. 2018; Yan et al. 2018) allow the tensile load to be transferred between two collinear bars inserted into a grouted metal sleeve. The couplers are generally made of mild steel, but also aluminium sleeves were proposed, such as the specimens of the AS series tested by Hua et al. (2014). The overall length and outer diameter of the grouted couplers generally do not exceed $20\varnothing_b$ and $4\varnothing_b$, respectively, with $\varnothing_b$

being the diameter of the spliced bar. The tensile capacity of the connection is ensured by the confining effect offered by the sleeve to the grout inside it, and by the grout to the spliced bars (Hua et al. 2014). In column-to-foundation connections, the bar couplers can be placed inside the footing or, alternatively, in the column base (Ameli et al. 2016). In both cases, global ductility is generally lower than that allowed by cast-in-place concrete construction, but, anyway, is generally adequate for use in moderate-to-high seismic zones. When the couplers are placed in the column base, the loss in ductility is attributed to the disruption introduced by the couplers to the plastic hinge zone of the column. However, damage localization occurs at the column-foundation interface only, allowing for a relatively simple and fast retrofitting. Alternative types of couplers are represented by threaded mechanical connectors. Cyclic load test results on a column-to-foundation joint using such connectors were recently presented by Dal Lago et al. (2016). Compared to monolithic solutions, the energy dissipation of this joint was smaller due to pinching in the hysteretic response, but the effective plastic hinge length was substantially the same.

Grouted duct connections make use of non-contact lap splices of the longitudinal reinforcement (Park 1995; FIB 2003; Rave-Arango et al. 2018). The bars protruding from one precast unit are grouted into corrugated steel ducts encased in the other unit. Adjacent to each duct one or more bars are present, lap-spliced to the outside of the duct. The experimental analyses conducted by Kuttab and Dougill (1988) and Zheng (1996) should be mentioned among the first researches on column-to-column grouted duct connections. Similar connections, but specifically tailored to column-to-foundation joints, were proposed and tested by Belleri and Riva (2012) and, more recently, by Popa et al. (2015). In these connections, analogous to that illustrated in Fig. 5-35 of FIB Bulletin No. 27 (FIB 2003), four projecting bars, embedded in the footing and protruding from it, are inserted into as many corrugated steel ducts placed at the corners of the column cross-section and then grouted. Two smaller-diameter bars are placed in the column adjacent to each duct. The lap splice of the projecting and smaller-diameter bars enables the load transfer mechanism between column and footing.

The experiments carried out by Belleri and Riva (2012) clearly showed the potentiality of grouted duct connections in term of ductility. The displacement capacity was favourably influenced by the confining effects of the metal ducts, which avoided bar buckling. The observed damage was mainly concentrated at the column-foundation interface. The authors then argued that post-seismic repair of these connections may be simpler than conventional cast-in-place or pocket foundation connections. This feature also suggested to the authors to use an unbonded length of projecting bars, to further increase ductility and reduce damage.

The experiments carried out by Popa et al. (2015) highlighted the effects due to axial load on column-to-foundation connections. In particular, they tested, up to 5% drift, one cast-in-place and two grouted duct specimens for an average compression stress of $0.16f_{cd}$ and $0.32f_{cd}$. For the greater axial load, the damage was more pronounced, but no bar buckling was observed. For all precast specimens, the final damage state was less severe than that obtained for the cast-in-place specimens.

Another connection system was recently proposed by Tullini and Minghini (2016) for column-to-column joints. In that proposal, the steel ducts were positioned along the sides of the column cross-section rather than at the corners, so allowing for the use of traditional reinforcement cages presenting longitudinal bars at both mid-side and corners of the cross-section. This feature is also present in the column-to-column connection shown in Fig. 5-90 of FIB Bulletin n. 78 (FIB 2016). However, in that case the reinforcement bars of the lower column are collinear with those of the upper column and must be bent inward to allow their insertion into the corrugated ducts of the upper column itself. Conversely, in the proposal by Tullini and Minghini (2016), the projecting bars are lap spliced with the bars of both lower and upper column. Therefore, a reduced amount of operations is required to assemble the two reinforcement cages.

The column-to-column connection proposed by Tullini and Minghini (2016) was subjected to five different load tests, including a direct tension test and cyclic shear test. In the former, failure took place far from the joint section, outside the bar splice region. In the latter, the shear force

resisted by the joint section was coincident with the pure shear resistance of the eight projecting bars, resulting unaffected by the cyclic loading protocol.

The reader is referred to Fig. 1 for a comparison among the connections tested by Zheng (1996), Belleri and Riva (2012), Popa et al. (2015) and Tullini and Minghini (2016).

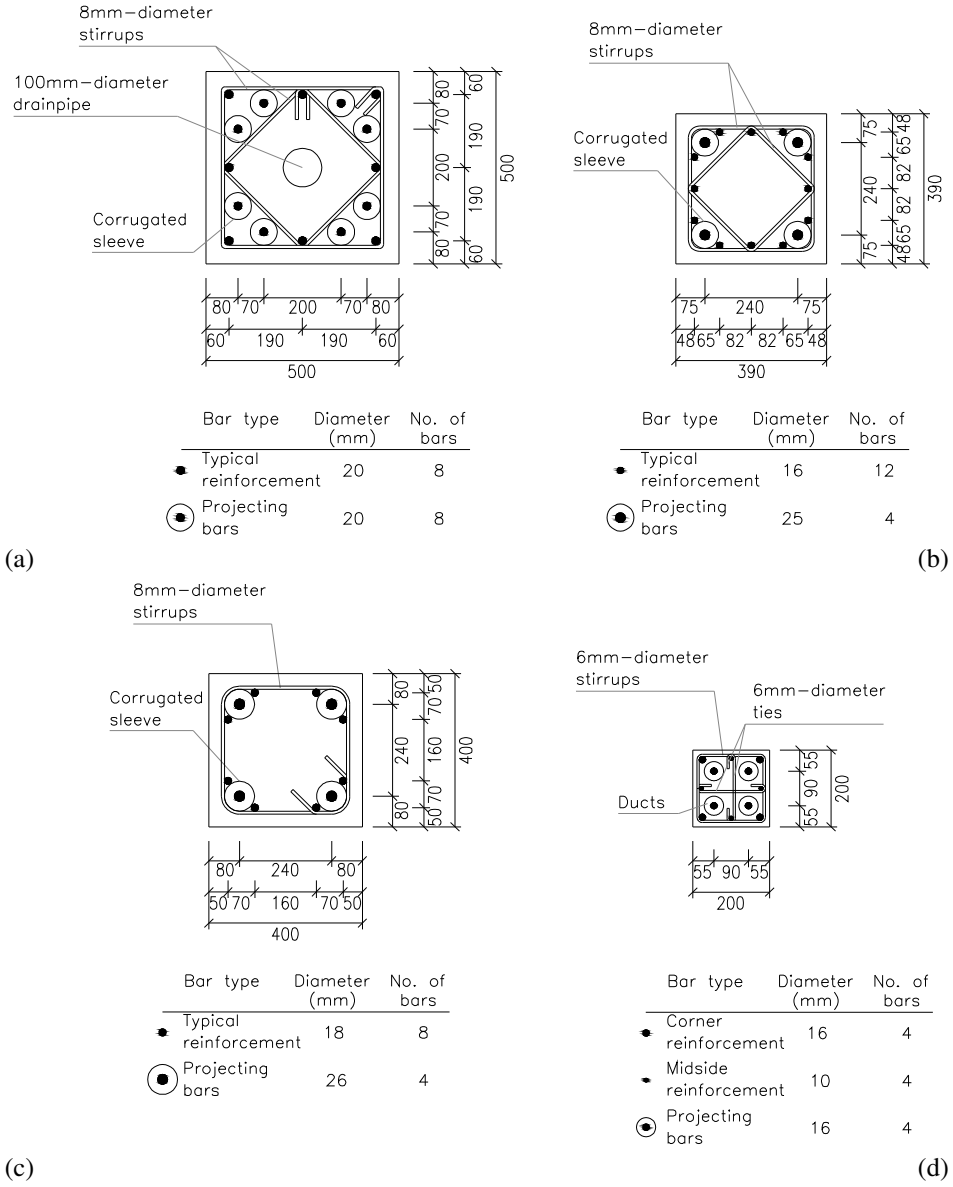

Fig. 1 Comparison between different grouted connections: typical column cross-section in the lap splice region for the connection systems proposed by (a) Tullini and Minghini (2016), (b) Popa et al. (2015), (c) Belleri and Riva (2012) and (d) Zheng (1996). Dimensions in mm

1.1. Novelty of the presented analysis

The aim of the present paper is to carry through with the experimental investigation of the connection system proposed by Tullini and Minghini (2016). In fact, the same column cross-

section, lap length of projecting bars, reinforcement ratio and detailing are considered, but they are applied to a column-to-foundation joint. The connection is suited for buildings and industrial structures.

In the research by Tullini and Minghini (2016), three different bending tests were carried out. In particular, the connection system was subjected to (1) monotonic and (2) cyclic bending tests, both in the absence of axial load, and to (3) a test in monotonic bending combined with axial compression. In this paper, the connection system was subjected to cyclic bending combined with axial compression. The test described hereinafter is then essential to give a full characterization of the grouted duct connection for potential applications in seismic areas. A comparison between this test and the previous one in monotonic bending with axial compression is presented in Sect. 4.4.2.

The adopted test configuration is analogous to that referred to as Case IV in user's manual of database provided by Pacific Earthquake Engineering Research Center (PEER 2004), with the axial load not passing through the intersection between column centreline and footing. The relevant test results, followed by considerations on ductility and dissipated energy, are reported hereinafter. In addition to the measurements of transverse deflection and longitudinal displacements at the column base, usually adopted in analogous tests to compute average strains and curvature (Belleri and Riva 2012), the shear slip at the column-foundation interface was measured during the test. To the authors' knowledge no research work considering the effects due to shear slip is available in the literature. The slip measurement was accounted for in evaluating the influence of second order effects, resulting in a modified expression for the axial load eccentricity with respect to that deduced from PEER Center's manual (PEER 2004). The slip was also included in calculations of column drift and plastic hinge length.

Section 5 reports the results of an analytical study aimed at interpreting the observed experimental behaviour. In particular, six models adopted mean values of the material properties and two other models adopted design values. The slip of the projecting bars within their ducts was

taken into account by means of an apparent strain or, alternatively, a pseudo stress-strain relationship.

Cyclic tests on the analogous cast-in-place connection were not repeated because widely reported in the literature (Belleri and Riva 2012; Popa et al. 2015; Liu et al. 2018).

2. DESCRIPTION OF THE COLUMN-TO-FOUNDATION CONNECTION

The full-scale test specimen is depicted in Fig. 2. The column (Fig. 2a) has a square cross-section with the side of 500 mm, is 3.7 m long and is connected with a 500 mm-thick foundation showing in plan dimensions 1.74×1.20 m (Fig. 2b).

Two HEB 500 steel profiles are used to delimit the footing along the shortest edges, so as to allow for the installation into the reaction frame. The footing principal reinforcement, parallel to the bending plane, is comprised of two layers of 20 mm-diameter bars welded to the webs of the steel profiles. Two layers of 16 mm-diameter bars are used in the orthogonal direction. The eight projecting bars, protruding from the foundation, have the diameter of 20 mm.

The most significant column cross-sections are depicted in Fig. 2b. The regular reinforcement is comprised of eight 20 mm-diameter bars positioned at mid-side and corners of the cross-section (cross-section D-D in Fig. 2b). The clear concrete cover is 42 mm, leading to a distance of 60 mm between the centroidal axis of the regular reinforcement and the concrete surface. Eight corrugated steel ducts, with outer diameter and thickness of 63 and 0.8 mm, respectively, are encased in the column so as to allow for the insertion of the projecting bars protruding from the foundation. The ducts are bent outwards to be injected later. The lap splice, enabling the stress transfer between projecting bars and regular column reinforcement, has the length of 1 m (Fig. 2a).

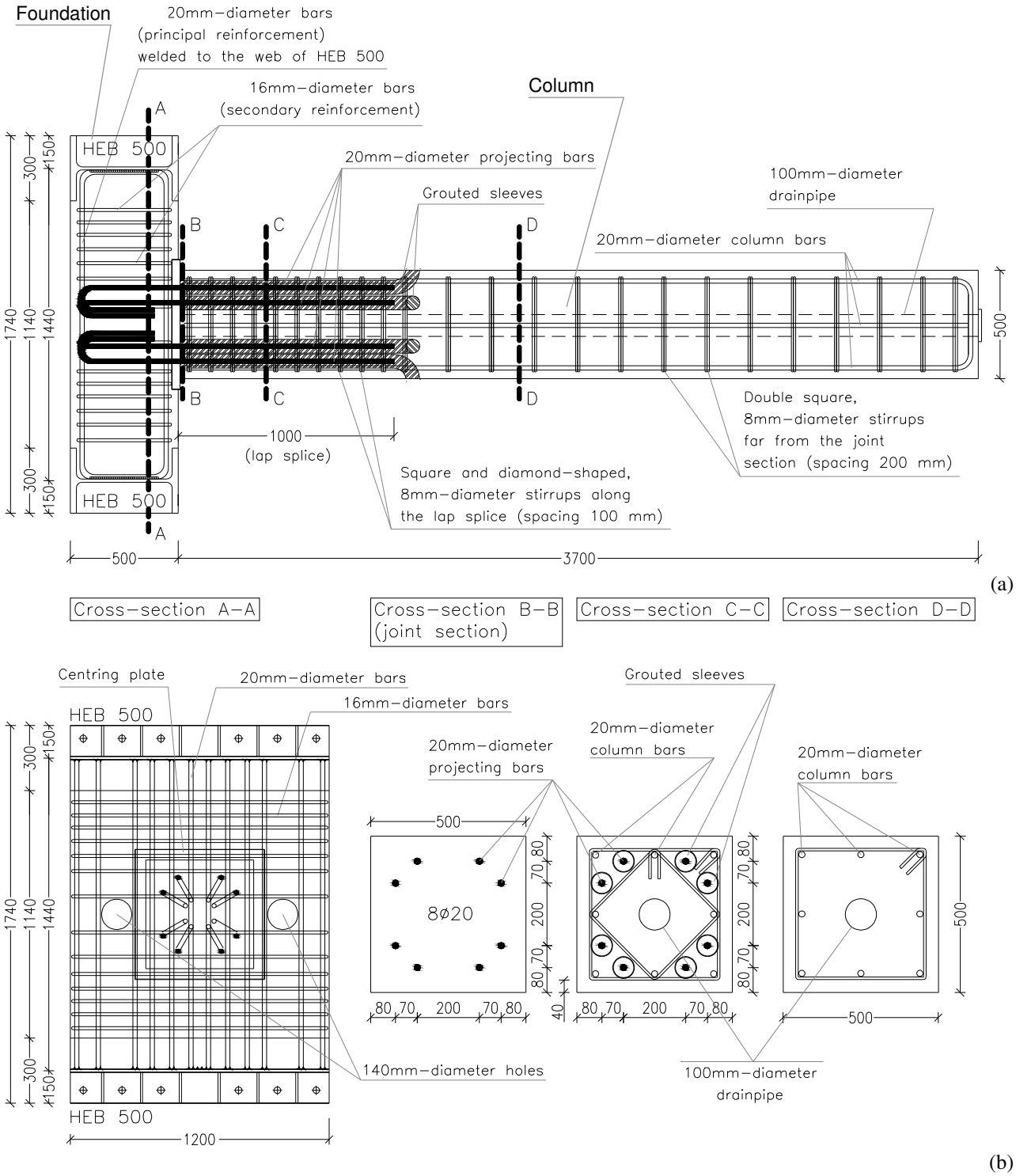

Fig. 2 Specimen used for the cyclic load test on the column-to-foundation connection: (a) side view of the reinforcement details and (b) relevant cross-sections. Dimensions in mm

The transverse column reinforcement is comprised of 100 mm-spaced square and diamond-shaped stirrups along the lap splice (cross-section C-C in Fig. 2b), and 200 mm-spaced pairs of square stirrups outside the lap zone. All stirrups are obtained from 8 mm-diameters deformed bars. The cross-section at the column-foundation interface (cross-section B-B in the Fig. 2b) is

characterized by the presence of the eight projecting bars only. This section will be referred to as the joint section. The minimum distance from the centroidal axis of the projecting bars to the concrete surface is of 80 mm.

Detail views of the reinforcement cages of footing and column are shown in Figs. 3a and 3b, respectively. The projecting bars can be observed in Fig. 3a. The two PVC tubes, having the diameter of 140 mm, will accommodate the Dywidag bars used for post-tensioning (see Sect. 4.3.1). The steel ducts and reinforcement details in the lap zone can be observed in Fig. 3b. The assembled specimen, with the grouted ducts, is shown in Figs. 3c.

The presence of a drainpipe in centroidal position inside the column (Figs. 1a, 2 and 3b) is quite common in Italian precast RC construction.

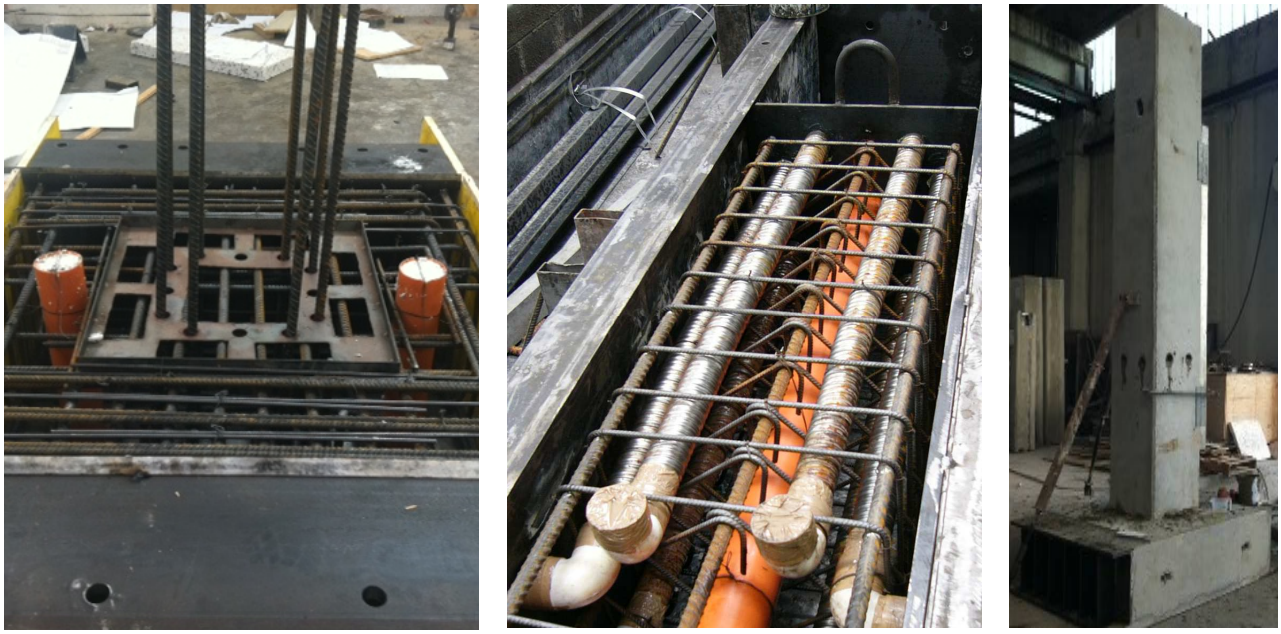

(a) (b) (c)

Fig. 3 Reinforcement cages of (a) foundation, with the eight projecting bars, and (b) column, with the corresponding corrugated steel sleeves; (c) assembled specimen with the sleeves just grouted

2.1. Design of the lap splice

The lap splice of the longitudinal column reinforcement (projecting and regular 20 mm-diameter bars) was designed based on Eurocode 2 provisions (CEN 2004a) for traditional deformed bars. The calculation of the lap splice length based on concrete strength class C40/50 is summarized in the Appendix. The design lap lengths for tension and compression result to be l_{0t} = 897 mm and l_{0c} = 828 mm, corresponding to 45 $\varnothing_b$ and 41 $\varnothing_b$, respectively. The adopted lap length of 50 $\varnothing_b$ satisfies the condition $l_0 \geq \max\{l_{0t}, l_{0c}\}$ required when the confining effect of the metal ducts is neglected. For the grouted duct connection shown in Fig. 6.1 reported by Bruggeling and Huyghe (1991), similar to those proposed by FIB (2003), Belleri and Riva (2012) and Popa et al. (2015), the recommended lap splice length is of 40 $\varnothing_b$.

With regard to the transverse reinforcement, along each of the two splice end regions of length $l_0/3$ = 333 mm, each regular longitudinal bar is engaged by 4 stirrups. Therefore, the total area of stirrups at the splice end regions satisfies the condition $\Sigma A_{st} \geq A_s$ (CEN 2004a), with A_s = 314 mm^2 being the cross-sectional area of one single spliced bar (see the Appendix).

3. MATERIAL PROPERTIES

3.1. Concrete

For each of the concrete mixes used for casting column and footing two 150 mm cubes were moulded to be tested in compression. In addition, two cubes were prepared from the concrete mix adopted for the injection grout. All cubes were tested in compression just before the cyclic test on the column-to-foundation connection. For each pair of cubes, the mean value $f_{cm,cube}(t)$ of the compressive strength at the corresponding age t and the value $f_{cm,cube}(28) = f_{cm,cube}(t)/\beta_{cc}(t)$ at t = 28 days are given in Table 1, where coefficient $\beta_{cc}(t)$ is computed in accordance with Eurocode 2 (CEN 2004a). According to Eurocode 2 (CEN 2004a), strength class C40/50 (characteristic cylinder

strength $f_{ck} = 40$ MPa) corresponds to the lowest strength class compatible with the measured strengths.

3.2. Reinforcing steel

The mechanical properties of reinforcing steel were estimated based on tension tests on 20 mm- and 8 mm-diameter bars used for longitudinal and transverse reinforcement, respectively. Three steel specimens were tested for each diameter. The mean values of the properties are given in Table 2, where E_{sm} indicates the elastic modulus, f_{ym} and f_{tm} are yield and ultimate strengths, respectively, and ε_{tm} is the strain corresponding to f_{tm}. These properties are consistent with steel class B450C recommended by the Italian standard (IMIT 2018), showing yield and ultimate design strengths $f_{yd} = f_{yk}/\gamma_s = 450/1.15 = 391$ MPa and $f_{td} = f_{tk}/\gamma_s = 540/1.15 = 470$ MPa.

Table 1 Concrete and grout compressive strengths obtained from tests on cubic specimens

Concrete type	Concrete age, t [days]	$\beta_{cc}(t)$	$f_{cm,cube}(t)$ [MPa]	$f_{cm,cube}(28)$ [MPa]
Foundation	81	1.086	62.2	57.3
Column	77	1.083	61.3	56.6
Grout	75	1.081	70.8	65.5

Table 2 Mean values of mechanical properties for reinforcing steel

Bar diameter [mm]	E_{sm} [GPa]	f_{ym} [MPa]	f_{tm} [MPa]	f_{tm}/f_{ym}	ε_{tm} [%]
8	Not available	518	616	1.19	11
20	198	556	665	1.20	11

4. CYCLIC TEST ON THE COLUMN-TO-FOUNDATION CONNECTION

In this Section, the results obtained from a quasi-static cyclic test on the column-to-foundation connection are reported. Quasi-static load testing is one of the mostly used experimental methods to assess performance and available ductility during major earthquakes (Park 1988).

Test layout, loading protocol, equipment and measuring systems are described in detail hereinafter. The experimental results are followed by an analytical interpretation of the cyclic response of the joint section.

4.1. Specimen layout

The specimen was placed on the reaction frame horizontally as shown in Fig. 4a. The cyclic load was applied to the column in the vertical plane at $L_\Delta = 2.8$ m from the joint section. Axial compression, N, was applied to the column end section. This configuration, analogous to Case IV described in PEER Center's manual (PEER 2004), is frequently adopted for cyclic load tests (Verderame et al. 2008a, b; Buratti et al. 2014).

The test layout at the initial, undeformed stage is illustrated in Fig. 5a. Assuming that a slip at the column-foundation interface may occur, the generic specimen configuration can be represented as in Fig. 5b, where:

- line *OEE'* represents the undeformed column axis (points *E* and *E'* are also reported in Fig. 5a);
- line *ACC'* represents the column axis translated upward of generic quantity *s*;
- segment *DAE* corresponds to column-foundation interface;
- quantities *e* and *s* represent axial load eccentricity and interface slip between column and foundation, respectively;
- line *AB* connects the centroid of the joint section (point *A*) to that of the cross-section subjected to the transverse load, at L_Δ from the column-foundation interface (point *B*). The centroid of the column end section (point *B'*) may be considered belonging to line *AB* (see Fig. 4c of Verderame et al. 2008a); the angle, θ, between lines *ABB'* and *ACC'* is the chord rotation and coincides with drift.

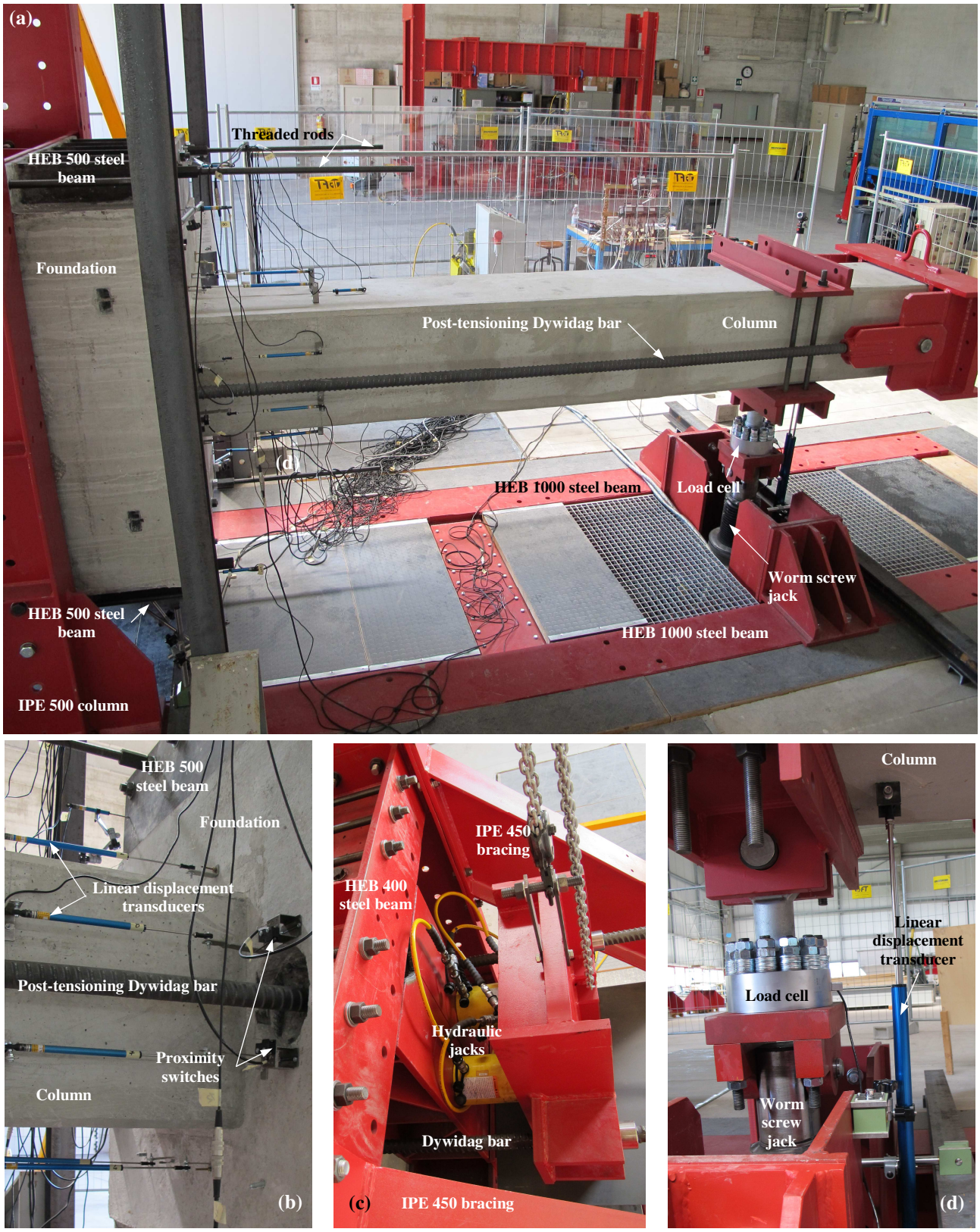

Fig. 4 Specimen installed into the reaction frame: (a) side view; detail views showing (b) the column-to-foundation connection with one of the Dywidag bars for post-tensioning and linear displacement transducers for strain measurements, (c) the two hydraulic jacks used to apply the constant axial load, and (d) the worm screw jack used to apply the cyclic transverse force

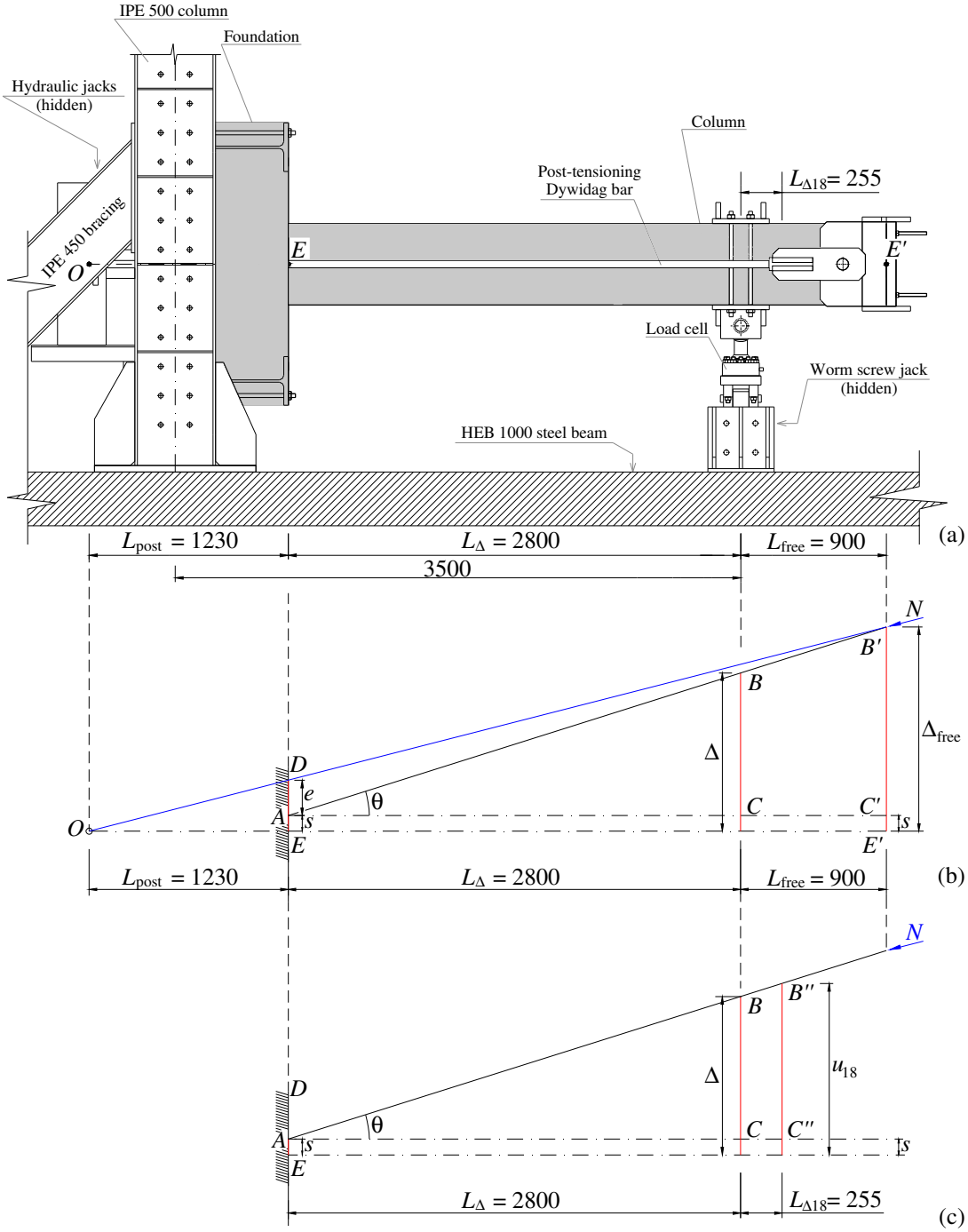

Fig. 5 Specimen layout: (a) side view (specimen in grey) and schematic for the evaluation of (b) second order effects due to N and of (c) deflection Δ based on measured deflection u_{18}

- line *ODB′* indicates the direction of compressive axial load *N* at a generic test stage and coincides with the direction of the two Dywidag bars used for post-tensioning the column;

- Δ and Δ_{free} are the transverse deflections, referred to the column axis in the initial (undeformed) state, experienced by the cross-section loaded by the cyclic actuator was acting and by the end section, respectively;

- L_{free} = 0.9 m is the distance between actuator and end section, whereas the line of application of *N* intersects the undeformed column axis behind the foundation, at a distance L_{post} = 1.23 m from the joint section.

Similarity between triangles *ABC* and *AB′C′* yields (Fig. 5b):

$$(\Delta - s)/L_{\Delta} = (\Delta_{free} - s)/(L_{\Delta} + L_{free}) \tag{1}$$

and transverse deflection Δ may then be expressed as:

$$\Delta = s + L_{\Delta}(\Delta_{free} - s)/(L_{\Delta} + L_{free}) \tag{2}$$

In addition, similarity between triangles *ODE* and *OB′E′* yields:

$$(e + s)/L_{post} = \Delta_{free}/(L_{post} + L_{\Delta} + L_{free}) \tag{3}$$

leading to the following expression for Δ_{free} in terms of *e* and *s*:

$$\Delta_{free} = L(e + s)/L_{post} \tag{4}$$

where $L = L_{post} + L_{\Delta} + L_{free}$. Solving Eq. (4) for *e* yields:

$$e = L_{post}\Delta_{free}/L - s \tag{5}$$

In similar experiments the interface slip was not considered (PEER 2004, Verderame et al. 2008a), resulting, at equal Δ_{free}, in an axial load eccentricity higher than that predicted by Eq. (5). Therefore, the presence of slip reduces the influence of second order effects. Substituting Eq. (4) into Eq. (2) leads to:

$$\Delta = s + [eL + (L_{\Delta} + L_{free})s]/[L_{post}(1 + L_{free}/L_{\Delta})] \tag{6}$$

The interface slip also influences the drift, which is computed as:

$$\theta = (\Delta - s)/L_\Delta \tag{7}$$

In analogy to what is done by PEER Center (2004) and Verderame et al. (2008a, b), an effective force taking account of second order effects is defined as:

$$F = F_\Delta - F_{\Delta 0} + Ne/L_\Delta \tag{8}$$

where F_Δ indicates the transverse force applied by the cyclic actuator and $F_{\Delta 0}$ is a correction term depending on the specimen self weight. This term, which was estimated based on the vertical reaction of an ideal constraint placed at distance L_Δ from the joint section, takes the values $F_{\Delta 0} = 15.8$ kN for the specimen being in the linear elastic range and $F_{\Delta 0} = 17.5$ kN after the formation of a plastic hinge at the column-to-foundation connection.

The experimental results will be presented in Section 4.4 in terms of F-Δ response, in accordance with several of the results collected in PEER Center's database (PEER 2004).

4.2. Loading protocol

The specimen was initially subjected to a compressive axial force N = 1700 kN, estimated on the basis of the gravitational loads expected to act on it, in a seismic load combination, in a parking garage made of precast RC elements. The value of N corresponds to $0.14 f_{cm} A_c$, where $A_c = 2.40 \times 10^5$ mm^2 is the area of the concrete cross-section and $f_{cm} = 50.9$ MPa is the mean cylinder strength of concrete estimated as $\lambda f_{cm,cube}$, with $f_{cm,cube} = 61.3$ MPa (Table 1) and $\lambda = f_{cm}/f_{cm,cube} = 0.83$ according to the Italian standard (IMIT 2018). Moreover, the axial force corresponds to the value of $0.31 f_{cd} A_c$, with f_{cd} being the design compressive strength for concrete evaluated for class C40/50 (see Sect. 3.1).

With a constant axial compression, a cyclic transverse deflection was applied to the column at a distance L_Δ from the joint section. The stroke rate was of 0.7 mm/min. The loading protocol adopted is graphically represented in Fig. 6 by a thin solid line (labeled "Δ").

A total of 19 loading cycles were carried out. The first 10 cycles were intended not to cause yielding of the reinforcing bars. The five target drifts of these cycles were, in the order of their application, ±0.1%, ±0.2%, ±0.5%, ±0.7% and ±0.8%, each one repeated one time only (ACI 2013). Then, 8 cycles were carried out with target drifts gradually increasing from 1% to 5%, with a step of 0.5% at each cycle. In the last cycle, the maximum drift attained was 5.3% (see Section 4.4). Therefore, 7 and 3 loading cycles were carried out with target drifts exceeding the allowable drifts defined by FEMA (2000) for Life Safety (2%) and Collapse Prevention (4%) performance levels, respectively.

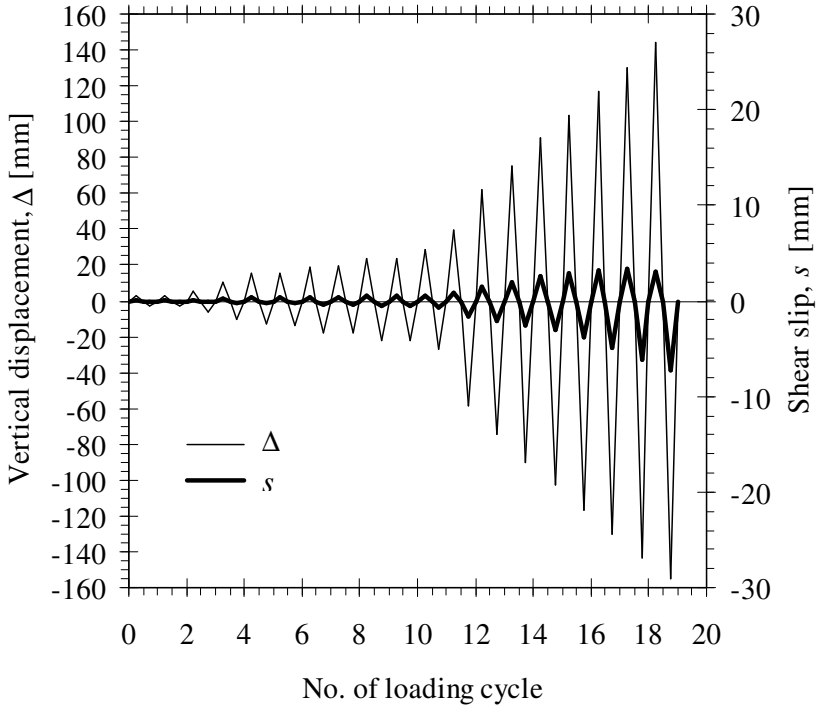

Fig. 6 Loading protocol in terms of deflection (Δ) of the column cross-section located at a distance L_Δ from the joint section, and interface slip (s) during the test

4.3. Testing equipment and measuring system

The test rig (Fig. 4) is comprised of two HEB 1000 steel beams (whose top flanges are visible in Fig. 4a) located below the pavement level and a plane frame, 3.5 m-high, bolted to the beam top flanges. This frame, constituted by two IPE 500 columns and two HEB 400 beams, is stiffened by two IPE 450 inclined bracings limiting out-of-plane deformations. To place the specimen on the reaction frame, the two HEB 500 steel beams enclosing the foundation were connected to the HEB

400 profiles of the frame using twelve 27 mm-diameter threaded rods (some of which shown on top right and top left of Figs. 4a and 4c, respectively).

4.3.1. Application and measurement of the axial load

The column axial load was applied by post-tensioning two 47 mm-diameter Dywidag bars arranged parallel to the vertical sides of the column (Fig. 4a). At the column end section, each of these bars was screwed to a steel fork, which, in turn, was hinged to a lid anchored to the column tip. At the opposite side, behind the foundation, the Dywidag bars were connected to a suitable anchoring element by means of 83 mm-diameter threaded sleeves.

A detail view showing one of the Dywidag bars passing through the foundation is reported in Fig. 4b. Note that, for each bar, two switches were used to warn if the hole's boundary had been excessively approached by the bar due to column deflection.

The posterior anchoring system is shown in Fig. 4c. Also shown in the figure are the two hydraulic jacks with the loading capacity of 1 MN used to tension the Dywidag bars. These jacks, connected in parallel to the same pump, were positioned with the base against a load transfer element in contact with the posterior surface of the foundation and the plunger acting on the steel element used to anchor the Dywidag bars.

The pressure in the oleodynamic circuit activating the jacks was measured using pressure transducers with the nominal capacity of 700 bar. Being the two jacks identical, the axial load was obtained as twice the measured pressure multiplied by the cylinder effective area as declared by the manufacturer.

4.3.2. Application and measurement of the cyclic transverse force

The time-history of the vertical deflection was imposed by an electromechanical worm screw jack with loading capacity of 500 kN, stroke of ±250 mm and maximum rate of 0.7 mm/s, accommodated into a steel supporting element bolted to the HEB 1000 beams of the reaction frame

(Fig. 4a). A Pi-shaped steel element, pinned to the jack, was used to support a 500 kN full-scale load cell with the nominal sensitivity of 2 mV/V (Fig. 4d). The cyclic force was transferred to the column by means of two stiffened steel plates positioned on the top and bottom sides (Fig. 4a).

4.3.3. Measurement of displacements and strains

Eighteen linear displacement transducers, in the following referred to as L*i* (*i* = 1, ..., 18), were used to measure absolute and relative displacements (Fig. 7).

As for the absolute displacements, seven transducers were used (in blue in Fig. 7a). Rigid body displacements of the specimen due to deformations of the reaction frame were measured by horizontal transducers L11 to L14 and vertical transducers L15 and L16. Transducers L11 to L16 are also shown in the frontal view of Fig. 7c. The same figure shows proximity switches S1 to S4 used to alert for an excessive approach of the Dywidag bars to the holes' boundaries. Transducer L18 (also shown in Fig. 4d) was used to measure the column vertical deflection (u_{18} in Fig. 5c) experienced by the cross-section located at a distance $L_{\Delta} + L_{\Delta 18} = 2800 + 255 = 3055$ mm from the joint section (Fig. 7a). In Fig. 5c, the same assumptions already adopted in Fig. 5b are used. In particular, straight line *ABB''* indicates the column axis at the generic test stage. For simplicity, the line of application of *N* is not shown in this case.

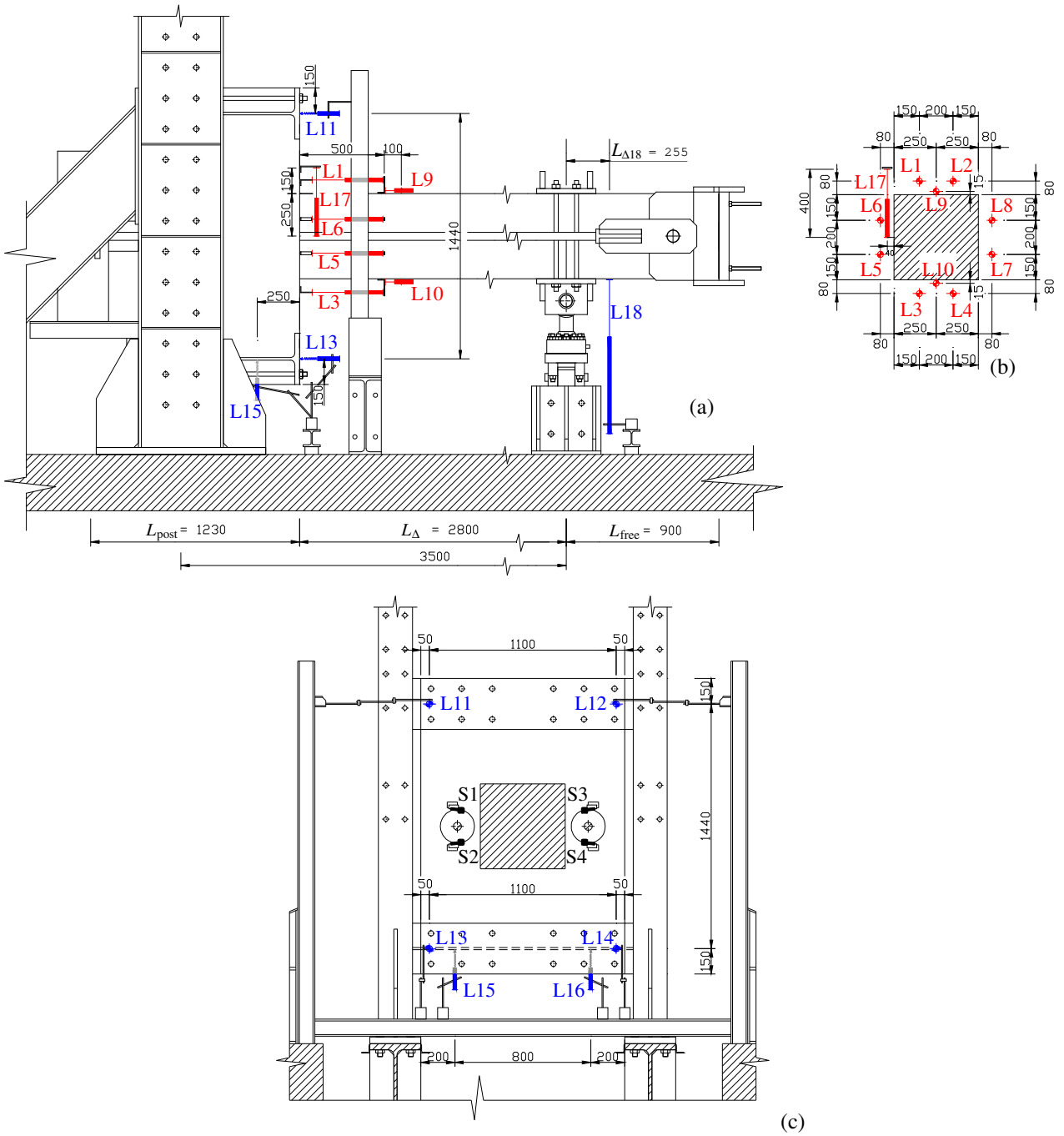

Fig. 7 Positions of the linear displacement transducers: (a) side view, (b) column cross-sectional view and (c) frontal view of the test setup. Dimensions in mm

From similarity between triangles *ABC* and *AB″C″* in Fig. 5c, deflection Δ turns out to be related with L18 measurement by the relation:

$$\Delta = s + L_{\Delta}\left(u_{18} - s\right)/\left(L_{\Delta} + L_{\Delta 18}\right) \tag{9}$$

All these transducers were attached, using magnets, to metal supports placed on the pavement of the laboratory, and therefore independent of the reaction frame.

As for the relative displacements, eleven transducers were used (in red in Fig. 7). Horizontal transducers L1 to L8 were positioned in proximity of the joint section as shown in Figs. 4b and 7a, b. In particular, two transducers for each column side were placed in correspondence of the grouted ducts. These transducers were used to measure average strains in the column region where plastic hinge formation was expected to occur. Other two horizontal transducers, i.e., L9 and L10, were positioned at the column top and bottom sides to measure average strains near the joint section, outside the plastic hinge region. For each of these transducers, the average strain was estimated from the following relation (i = 1, ..., 10):

$$\varepsilon_i = u_i / b_i \tag{10}$$

where u_i is the displacement measured by the transducer and b_i the initial distance between the two points where the transducer is connected to the specimen. According with Fig. 7a, b_i = 500 mm for i = 1, ..., 8 and b_i = 100 mm for i = 9 and 10. Vertical displacement transducer L17 was used to measure the shear slip between column and foundation at the joint section, associated with the shear deformation of the projecting bars.

All displacement transducers, as well as pressure transducers (see § 4.3.1) and load cell (§ 4.3.2), were connected with the data acquisition system via a power unit operating at 50 mA and 10 V. A LabVIEW code (NI 2015) was developed to display all measurements in real-time.

The detection of the slip of the projecting bars, which may be significant for this kind of prefabricated structural elements (Raynor et al. 2002), needs strain gauges connected to both projecting bars and metal ducts along the entire lap length. However, to avoid possible detrimental effects on the bond strength of the bars, strain gauges were not used in this research. The average strains (Eq. (10)) may locally differ from the actual strains, but they are usually adopted when strain gauges are not used (Belleri and Riva 2012).

4.4. Experimental results

The F_Δ–Δ experimental diagram, with F_Δ (see Eq. (8)) being the cyclic transverse force applied by the actuator not including the correction terms for specimen self weight ($F_{\Delta 0}$) and second order effects (Ne/L_Δ), is reported in blue in Fig. 8a. The non-symmetry of the plot is due to the horizontal configuration of the specimen. In fact, self weight acts according to or against the actuator depending on the sign of the deflection. This is the reason why the maximum absolute value of F_Δ attained during the downward half-cycles (negative force values) is approximately 18% smaller than that attained upward (positive force values).

The cyclic diagram shown in Fig. 8a with a black line refers to the F–Δ response of the specimen, where force F, according to Eq. (8), includes both second order contribution and correction for self weight. Therefore, F is representative of the total bending resistance of the joint section (see Eq. (11)). As expected, due to the symmetry of the joint section (see cross-section B-B in Fig. 2), the F-Δ plot is substantially symmetric with respect to the origin. The softening effect observed in the F-Δ plot indicates a deterioration of the bending strength mainly related with the spalling of the concrete cover in the column.

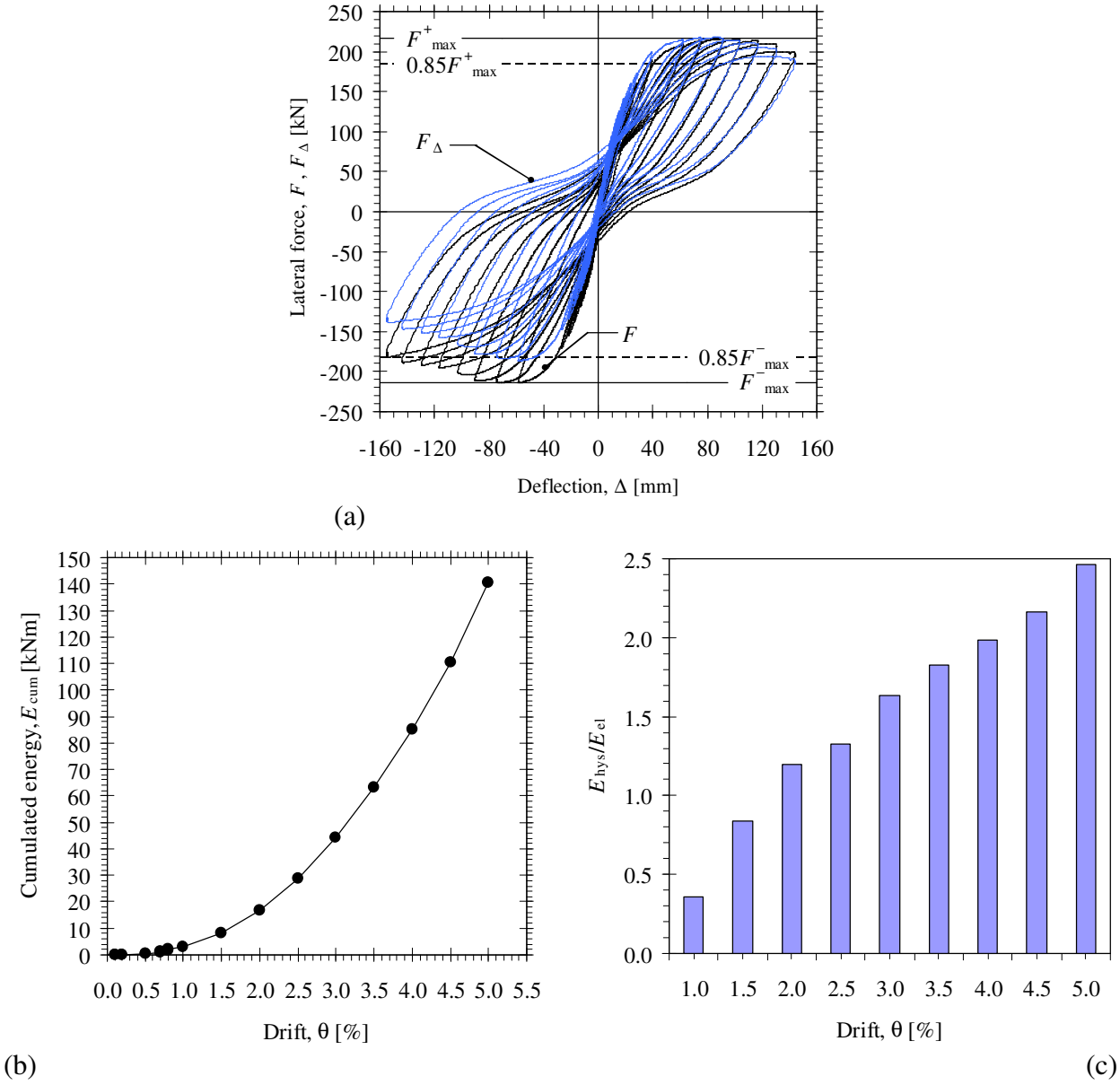

Fig. 8 Test results: (a) cyclic diagrams of applied (F_Δ) and effective (F) forces versus deflection, (b) cumulated hysteretic energy and (c) nondimensional hysteretic energy versus drift

The maximum effective force resisted by the column-to-foundation connection was $F_{max} = 216.2$ kN. The test was stopped at the end of the 19th loading cycle, in which the strength attained the value $F_u = 182.0$ kN $= 0.85F_{max}$, where index "u" stands for ultimate. A drop of 15% with respect to the peak strength corresponds to one of the Ultimate Limit State (ULS) conditions stated by CEN (2004b). The maximum values of deflection and slip were $\Delta_u = 155.1$ mm and $s_u = 7.3$ mm, respectively, resulting in a drift $\theta_u = 5.3\%$. Figure 6 shows the comparison between

the shear slip at the column-foundation interface (thick solid line) and the vertical deflection. It can be observed that *s* started to develop for $\Delta \geq 60$ mm (i.e., for drift $\theta \geq 2\%$). The extent of the shear slip is expected to depend on the axial compression, which activates friction at the column-foundation interface. The smaller the axial compression, the greater the importance of *s* may be. This feature will deserve particular attention in future researches.

The deflected configuration of the specimen during the last downward half-cycle is shown in Fig. 9a. In analogy with several experimental tests on precast column-to-foundation connections (Ameli et al. 2016; Belleri and Riva 2012; Dal Lago et al. 2016), the damage was mainly localized in proximity of the joint section, where yielding and hardening of the projecting bars were attained and complete spalling of the concrete cover took place on the column bottom (Fig. 9b) and top sides (Fig. 9c,d). The confinement provided by the stirrups on the concrete core along the splice region, and by the corrugated ducts on the inside grout, avoided the instability of the longitudinal reinforcement.

The pinching shown in the F-Δ plot of Fig. 8a was due to a combination of causes. The extent of the axial compression was one of these causes. In fact, the force-deflection plot for the cyclic test described by Tullini and Minghini (2016), where axial load was absent, is not pinched. Moreover, the significant plastic deformations achieved for $\theta \geq 2\%$ in the projecting bars may have played a role in narrowing the loading cycles. In severely yielded bars, indeed, after the attainment of the maximum deflection in a given cycle and the following unloading phase, plastic tensile strain was still present. During the initial phase of reloading in the opposite direction, and up to closing of previous cracks, compression was then resisted only by projecting bars. As a consequence, the reduced global stiffness might have led to pinching. An analogous explanation to pinching was given by Popa et al. (2015). Another possible cause of pinching may have been the progressive damage of the thin grout layer which was present at the column-foundation interface. This feature was highlighted also by Belleri and Riva (2012) for their specimens GS4 and GS4B.

A video of the test (velocity increased 100 times) is provided, attached to the electronic version of the present paper to which the interested reader is referred to.

Fig. 9 (a) Column deflected configuration during the last half-cycle; and (b) bottom and (c, d) top sides of the column in proximity of the joint section at the end of test

4.4.1. Dissipated energy

The hysteretic energy (E_{hys}) dissipated during each test is defined as the area contained by the experimental F-Δ cycles and may be estimated by applying the trapezoidal rule to the plot of Fig. 8a. The cumulated hysteretic energy at the kth cycle, reported in Fig. 8b versus drift, is defined as $E_{cum,k} = \sum_{i=1}^{k} E_{hys,i}$. At the end of test, $E_{cum} = 140$ kNm was achieved. The amount of dissipated

energy strongly depends on the loading protocol adopted. The last 13 cycles of the displacement history shown in Fig. 6 are similar to the loading protocol used by Popa et al. (2015), comprised of 13 cycles at a drift ranging between 0.5% and 5%. The cumulated energy E_{cum} = 140 kNm is quite close to those reported by Popa et al. (2015) for cast-in-place specimen CIP2. Such a comparison is believed to be meaningful, because specimen CIP2 showed characteristics comparable to those of the present specimen (Table 3).

The dissipated energy per cycle is also presented in nondimensional form in Fig. 8c for $\theta \geq 1\%$, where E_{el} indicates the elastic energy per half-cycle, i.e., one half of the maximum displacement times the corresponding effective force. An estimate of the equivalent viscous damping ratio may be obtained as $E_{hys}/(4\pi E_{el})$, leading to 20% in the last loading cycle.

Although its tendency to pinching, the cyclic diagram in Fig. 8a presents a stable hysteretic behavior.

Table 3 Specimen characteristics and some test results for present specimen and one of the cast-in-place specimens tested by Popa et al. (2015). The compared quantities are: shear span (L_Δ and L_Δ/H ratio); reinforcement ratio of the joint section (ρ_{lj}); nondimensional axial load ($N/(A_c f_{cd})$); maximum resisted lateral force (F_{max}); cumulated hysteretic energy at the end of test (E_{cum}) and drift ductility ($\mu_\theta = \theta_u/\theta_y$)

Specimen	$L_\Delta(L_\Delta/H)$ [m]([-])	ρ_{lj} [%]	$N/(A_c f_{cd})$ [-]	F_{max} [kN]	E_{cum} [kNm]	$\mu_\theta = \theta_u/\theta_y$ [-]
CIP2 in Popa et al. (2015)	2.0(5.1)	1.29	0.32	190	145	5.00
Present specimen	2.8(5.6)	1.01	0.31	216	140	4.42

4.4.2. Moment-average curvature diagram for the joint section

The bending moment at the joint section, accounting for the second order effects, is given by the following equation:

$$M_j = FL_\Delta \tag{11}$$

with F being the effective transverse force obtained from Eq. (8). According with the positions of transducers reported in Fig. 7b, the average curvature may be evaluated, under the plain section hypothesis, from the following relation:

$$\chi_{j,A} = (\varepsilon_{34} - \varepsilon_{12})/d_A \tag{12}$$

or from the alternative relation:

$$\chi_{j,B} = (\varepsilon_{57} - \varepsilon_{68})/d_B \tag{13}$$

where ε_{12}, ε_{34}, ε_{57} and ε_{68} are the mean values of average strains obtained from Eq. (10) for the following pairs of displacement transducers: (L1, L2); (L3, L4); (L5, L7); and (L6, L8), respectively. Quantities d_A = 660 mm and d_B = 200 mm (Fig. 7b) are the vertical distances between transducers L1 and L3 (or, equivalently, L2 and L4), and between transducers L5 and L6 (or, equivalently, L7 and L8), respectively.

Average strain in the top layer (subscript 't') of projecting bars may be evaluated from the following alternative equations:

$$\varepsilon_{stA} = \varepsilon_{12} + \chi_{j,A} d_{stA} \tag{14}$$

$$\varepsilon_{stB} = \varepsilon_{68} - \chi_{j,B} d_{stB} \tag{15}$$

where d_{stA} = 160 mm and d_{stB} = 70 mm are the distances between top projecting bars and pairs of displacement transducers (L1, L2) and (L6, L8), respectively. Similarly, average strain in the bottom layer (subscript 'b') of projecting bars may be written as:

$$\varepsilon_{sbA} = \varepsilon_{12} + \chi_{j,A} d_{sbA} \tag{16}$$

$$\varepsilon_{sbB} = \varepsilon_{68} + \chi_{j,B} d_{sbB} \tag{17}$$

where d_{sbA} = 500 mm and d_{sbB} = 270 mm are the distances between bottom projecting bars and pairs of transducers (L1, L2) and (L6, L8), respectively.

Average concrete strains follow from similar relationships. For example, the strain at the top side of the column is given by:

$$\varepsilon_{ctA} = \varepsilon_{12} + \chi_{j,A} d_{ctA} \tag{18}$$

$$\varepsilon_{ctB} = \varepsilon_{68} - \chi_{j,B} d_{ctB} \tag{19}$$

whereas the strain experienced by the bottom side may be written as:

$$\varepsilon_{cbA} = \varepsilon_{12} + \chi_{j,A} d_{cbA} \tag{20}$$

$$\varepsilon_{cbB} = \varepsilon_{68} + \chi_{j,B} d_{cbB} \tag{21}$$

where (Fig. 7b) d_{ctA} = 80 mm, d_{ctB} = 150 mm, d_{cbA} = 580 mm and d_{cbB} = 350 mm.

Equations (12) and (13) led to substantially coincident curvature values. Therefore, the curvature at the joint section will be hereinafter defined as the average between $\chi_{j,A}$ and $\chi_{j,B}$ and simply referred to as χ_j. At the same time, average bar and concrete strains will be defined as $\varepsilon_{st} = (\varepsilon_{stA}+\varepsilon_{stB})/2$, $\varepsilon_{sb} = (\varepsilon_{sbA}+\varepsilon_{sbB})/2$, $\varepsilon_{ct} = (\varepsilon_{ctA}+\varepsilon_{ctB})/2$ and $\varepsilon_{cb} = (\varepsilon_{cbA}+\varepsilon_{cbB})/2$.

The records of displacement transducers L1 to L8 were also used to estimate the average column curvature in the horizontal plane, $\chi_{j\perp}$, produced by an unintended out-of-verticality of the applied transverse force. Yet, curvature $\chi_{j\perp}$ always remained one order of magnitude smaller than curvature χ_j.

Average strains ε_{st} and ε_{sb} in the projecting bars are reported in Fig. 10 versus deflection (units in the plot: ‰). The maximum tensile strain, attained during the last downward half-cycle, was ε_{st} = 2.84%.

The maximum concrete compressive strain, obtained for the bottom fibre from the average between Eqs. (20) and (21) immediately before the concrete spalling, resulted to be 0.52% (minus sign omitted, here and in the following, for simplicity of notation). After spalling (Fig. 9b, c) the maximum compressive strains must be referred to the confined concrete core. For example, with regard to the concrete core dimensions reported in the Appendix, bottom concrete strain may still be written in the form of Eqs. (20)-(21), provided that distances d_{cbA} and d_{cbB} are replaced with $d_{ccbA} = d_{cbA} - (H - h_0)/2 = 534$ mm and $d_{ccbB} = d_{cbB} - (H - h_0)/2 = 304$ mm, respectively. With these

substitutions, the maximum compressive strain at the bottom of the confined core, obtained again from the average between Eqs. (20) and (21), resulted to be 1.35%.

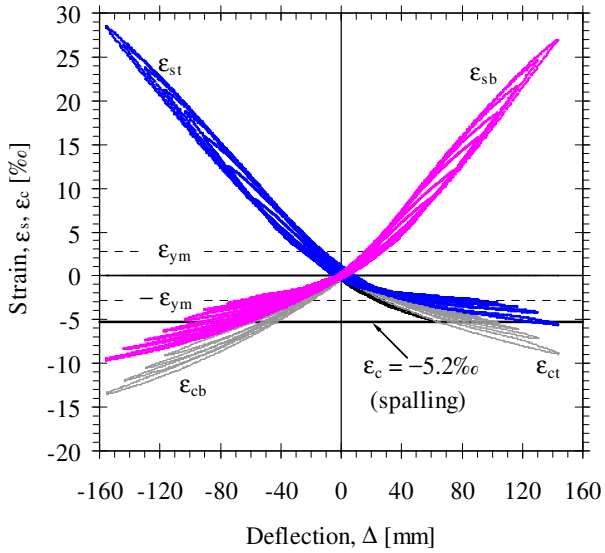

Fig. 10 Joint section deformability: average strains in top (ε_{st}) and bottom (ε_{sb}) projecting bars and average concrete compressive strains at top (ε_{ct}) and bottom (ε_{cb}) column sides

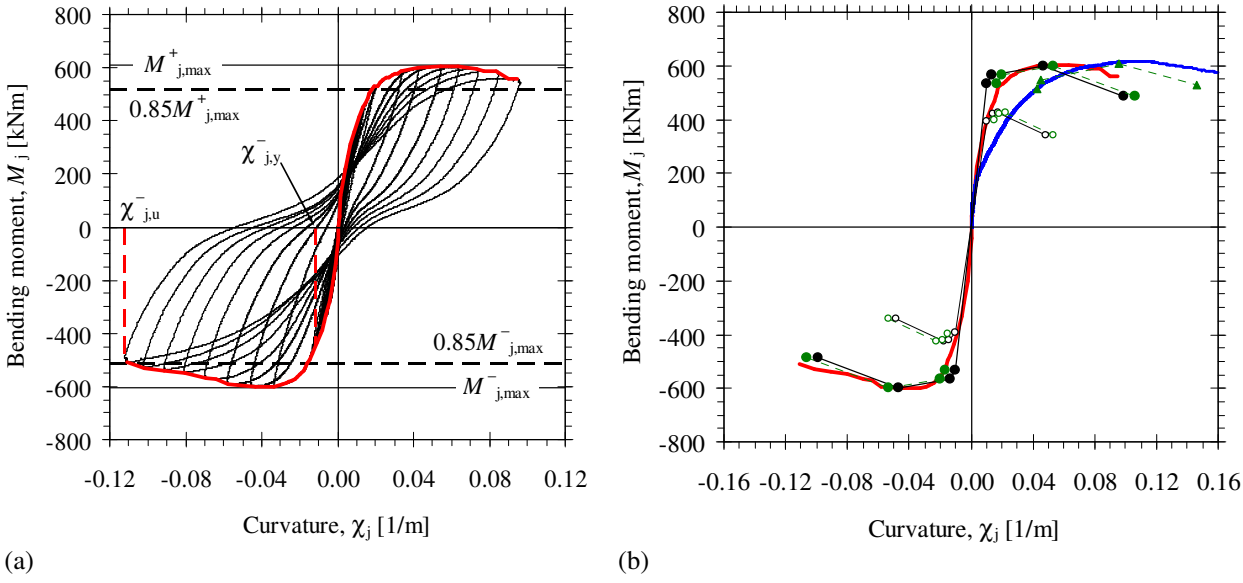

Fig. 11 Bending moment resisted by the joint section: (a) experimental cyclic diagram of moment versus curvature; and (b) analytical moment-curvature diagrams obtained from models (see Table 3): M_MS (green solid triangles); C_M (black solid circles); C_MS (green solid circles); C_D (black open circles) and C_DS (green open circles). Red curve in the two figures represents the envelope diagram of the cyclic response. Blue line in (b) represents the experimental diagram obtained by Tullini and Minghini (2016) from a monotonic test

This value is approximately 4 times larger than the conventional ultimate strain for unconfined concrete, equal to 0.35%, and 2.6 times larger than the maximum concrete strain achieved immediately before spalling. Top and bottom concrete strains obtained both before and after spalling are also reported in Fig. 10.

The cyclic diagram of bending moment M_j versus average curvature χ_j is reported in Fig. 11a. Also reported in the same figure is the envelope of the hysteresis loops (red solid line). The maximum bending moment resisted by the joint section, i.e., $M_{j,max} = F_{max}L_\Delta = 605.4$ kNm, was obtained in correspondence of curvature $\chi_{j,max} = 0.0542$ m^{-1}. At the conventional ULS, i.e., for $M_{j,u} = 0.85F_{max}L_\Delta = 514.6$ kNm, average curvature was $\chi_{j,u} = 0.1119$ m^{-1}.

The envelope diagram is reported again in Fig. 11b, where a comparison with the test in monotonic bending combined with axial compression described by Tullini and Minghini (2016) (blue line) is presented. The compressive axial force used in that investigation was approximately the same as in the present case. The maximum bending resistance of the monotonic response was only 2.3% larger than that of the cyclic response. This very small difference may be due to different material properties for the two specimens rather than to the influence of cyclic loading. The most significant feature of the comparison is the greater flexural deformability shown by the monotonic case, which is evident starting from a bending moment approximately equal to 30% of the peak flexural resistance. Tullini and Minghini (2016) ascribed this deformability to the slip between grouted bars and surrounding concrete, leading to a maximum recorded tensile strain in the projecting bars approximately 70% larger than that predicted by section analysis. It is worth noting that also Raynor et al. (2002) showed that bars in ducts may exhibit larger slip values when they are loaded monotonically. This feature appears not only in the post peak response but also in the proximity of bar yielding. It is believed that applying alternate tensile and compressive loads to the projecting bars may compact the grout into the steel ducts, with the effect of limiting the bar slip. Conversely, when projecting bars are subjected to monotonic tension, this effect is absent and bar slip becomes significantly larger. Future researches will be devoted to this aspect too.

5. DISCUSSION

To interpret the experimental results of the monotonic test described by Tullini and Minghini (2016) and of the cyclic test described in this paper, analytical moment-curvature diagrams for the joint section were evaluated using six different models (subscript 'a', in the following, will indicate analytical quantities). The results of these calculations are reported in Fig. 11b and in Table 4, where model acronyms stand for: Monotonic test, Mean properties (M_M); Monotonic test, Mean properties with bar Slip (M_MS); Monotonic test, Mean properties with bar Slip accounted for via a Pseudo stress-strain law (M_MP), see Ameli and Pantelides (2017); Cyclic test, Mean properties (C_M); Cyclic test, Mean properties with bar Slip (C_MS); Cyclic test, Mean properties with bar slip accounted for via a Pseudo stress-strain law; Cyclic test, Design properties (C_D); and Cyclic test, Design properties with bar Slip (C_DS).

Variations in the axial load occurred during the monotonic test were accounted for in calculations. For example, for models M_M and M_MS, at yielding and peak resistance the axial load was assumed to be 1620 and 1741 kN, respectively. Conversely, in models C_M, C_MS and C_MP the axial load was kept constantly equal to 1700 kN.

Table 4 Computed responses of the joint section: tensile strain in the outer reinforcement layer (see footnote [d]), maximum concrete compressive strain (ε_{ca}), curvature (χ_{ja}), bending moment (M_{ja}) and effective force (F_a)

Model	Computed quantity	Unit	Points of M_{ja}-χ_{ja} diagrams			
			1st yielding[a]	2nd yielding[b]	Peak strength	Ultimate strength[c]
M_M	ε_{sa}[d]	[‰]	2.61	3.45	19.9	30.4
	$\lvert\varepsilon_{ca}\rvert$	[‰]	1.33	1.58	6.20	10.1
	χ_{ja}	[‰/m]	9.39	12.0	62.2	108
	M_{ja}	[kNm]	515	547	610	530
	F_a	[kN]	184	195	218	189
M_MS	ε_{ssa}[d]	[‰]	16.7	17.5	34.0	44.5
	$\lvert\varepsilon_{ca}\rvert$	[‰]	1.33	1.58	6.20	10.1
	χ_{ja}	[‰/m]	42.9	45.5	95.7	146
	M_{ja}	[kNm]	515	547	610	530
	F_a	[kN]	184	195	218	189
M_MP	ε_{pa}[d]	[‰]	16.6	21.1	22.2	32.6
	$\lvert\varepsilon_{ca}\rvert$	[‰]	4.48	5.66	6.20	10.1
	χ_{ja}	[‰/m]	50.2	63.7	67.5	114
	M_{ja}	[kNm]	550	572	592	526
	F_a	[kN]	197	204	211	188
C_M	ε_{sa}[d]	[‰]	2.81	3.75	14.5	27.1
	$\lvert\varepsilon_{ca}\rvert$	[‰]	1.56	1.88	5.19	9.88
	χ_{ja}	[‰/m]	10.4	13.4	46.8	98.8
	M_{ja}	[kNm]	534	568	599	488
	F_a	[kN]	191	203	214	174
C_MS	ε_{ssa}[d]	[‰]	5.62	6.56	17.3	29.9
	$\lvert\varepsilon_{ca}\rvert$	[‰]	1.56	1.88	5.19	9.88
	χ_{ja}	[‰/m]	17.1	20.1	53.5	106
	M_{ja}	[kNm]	534	568	599	488
	F_a	[kN]	191	203	214	174
C_MP	ε_{pa}[d]	[‰]	5.62	7.32	15.2	28.1
	$\lvert\varepsilon_{ca}\rvert$	[‰]	2.33	2.89	5.19	9.88
	χ_{ja}	[‰/m]	18.9	24.3	48.5	90.3
	M_{ja}	[kNm]	555	581	592	517
	F_a	[kN]	198	207	212	184
C_D	ε_{sa}[d]	[‰]	1.96	2.94	3.85	9.31
	$\lvert\varepsilon_{ca}\rvert$	[‰]	2.29	2.96	3.50	8.68
	χ_{ja}	[‰/m]	10.1	14.1	17.5	48.1
	M_{ja}	[kNm]	395	422	425	340
	F_a	[kN]	141	151	152	122
C_DS	ε_{ssa}[d]	[‰]	3.91	4.90	5.80	11.3
	$\lvert\varepsilon_{ca}\rvert$	[‰]	2.29	2.96	3.50	8.68
	χ_{ja}	[‰/m]	14.8	18.7	22.2	53.3
	M_{ja}	[kNm]	395	422	425	340
	F_a	[kN]	141	151	152	122

Notes:

[a] 1st yielding refers to the achievement of yielding in tension for the outer bars;

[b] 2nd yielding refers to the achievement of yielding in tension for the bars at 350 mm from the most compressed fibre;

[c] Ultimate strength is the flexural strength of the joint section after spalling of the concrete cover;

[d] ε_{sa} indicates bar strain computed neglecting bar slip; ε_{ssa} and ε_{pa} indicate bar strains computed considering bar slip via apparent bar strain and pseudo stress-strain law, respectively.

5.1. Models neglecting the bar slip

Mean values of material properties were used for both concrete and steel. A parabola-rectangle constitutive relationship, with cylindrical strength f_{cm} = 57.9 MPa for the monotonic test (see Table 1 reported by Tullini and Minghini 2016) and f_{cm} = 50.9 MPa for the cyclic test (see Table 1 in this paper), was adopted for concrete in compression. The transition between parabolic and rectangular parts of the constitutive relationship was assigned, as usual, the strain value $\varepsilon_{c2} = 0.20\%$. The ultimate concrete strains were assumed to be 0.62% and 0.52% for monotonic and cyclic test, respectively, corresponding to the maximum compressive strains obtained experimentally before concrete spalling (see Sect. 4.4.4 in Tullini and Minghini 2016, and Sect. 4.4.2 in this paper). The final descending branch of the moment-curvature diagrams was obtained by modifying geometry and properties of the concrete section. After the attainment of the peak flexural resistance, the concrete cover was considered to be removed from the column cross-section and increased compressive strength and strains were defined for the confined core contained by the stirrups. Increased concrete strength f_{ccm}, strain ε_{c2c} at the attainment of the peak strength, and ultimate strain ε_{cu2c} were estimated according to Eurocode 2 (CEN 2004a). The effective lateral compressive stress due to confinement was estimated from $\sigma = \alpha\sigma_0$ (CEB 1998), with σ_0 and α being ideal, uniformly distributed confining stress and confinement effectiveness factor, respectively. The procedure used for the calculation of ultimate curvature is detailed in the Appendix.

For the longitudinal reinforcing steel, an elastic-plastic relationship with linear hardening was adopted. The mean values for Young's modulus, yield and ultimate strengths, and ultimate strain for the projecting bars were deduced from the results of tension tests (see Table 2 reported by Tullini and Minghini 2016, and Table 2 in this paper).

The calculated moment-curvature diagram for the monotonic load case (3rd and 4th rows of Table 4, model M_M) strongly underestimates the deformability observed in the test. For clarity, the corresponding curve, too distant from the experimental curve, is not reported in Fig. 11b. The too small, unacceptable curvature values essentially depend on calculated steel strains which do not

account for the slip experienced by the projecting bars. For example, at the peak strength, the calculated steel strain $\varepsilon_{sa} = 1.99\%$ (1st row in Table 4, model M_M) is only 58% the experimental average strain $\varepsilon_{sm} = 3.40\%$ (see Sect. 4.4.3 in Minghini and Tullini 2016).

For the cyclic load case (model C_M in Table 4), the calculated curvature still is underestimated, even if the approximation of the experimental moment-curvature diagram is better than for the monotonic load case. The calculated curve is plotted in Fig. 11b, where black solid circle data points correspond to the numerical values reported in Table 4 for 1st and 2nd yielding, peak strength and ultimate strength. At the peak strength, the difference between measured and predicted bar strains is about 0.28% ($\approx \varepsilon_y$), indicating a smaller influence of the bar slip compared with the monotonic test.

5.2. Models accounting for the bar slip via an apparent strain

Due to the choice of using linear displacement transducers to obtain averaged strains, displacement u_i recorded by the i-th instrument will contain, in general, two components in a unique measure: the displacement associated with actual strain distribution of the bar along length b_i, and the bar slip with respect to the surrounding concrete. The latter contribution gives rise to an apparent bar strain, $\varepsilon_{s,app}$. Therefore, the curvature of the joint section evaluated as (see Fig. 12)

$$\chi_{ja} = (|\varepsilon_{ca}| + \varepsilon_{ssa})/d \,, \tag{22}$$

will result increased compared with the models neglecting the bar slip. In the previous equation, ε_{ca} is the concrete strain at the most compressed fibre, $\varepsilon_{ssa} = \varepsilon_{sa} + \varepsilon_{s,app}$ the total strain of the outer projecting bars, and $d = 374$ mm (see the Appendix) or 420 mm depending on whether concrete spalling has occurred or not, respectively.

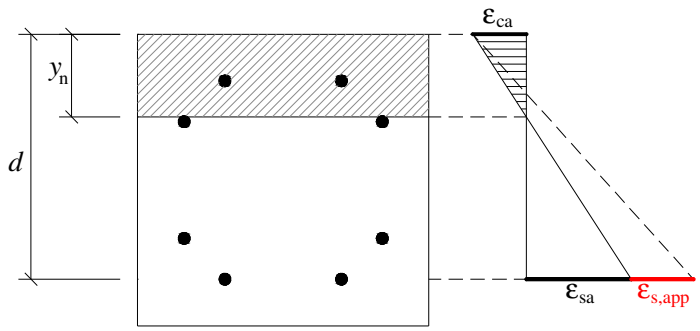

Fig. 12 Apparent bar strain due to slip (in red)

For the monotonic load case, the apparent bar strain was defined as

$$\varepsilon_{s,app} = \varepsilon_{sm} - \varepsilon_{sa} = 1.41\% = 5.4\varepsilon_{ym}, \tag{23}$$

where $\varepsilon_{sm} = 3.40\%$ is the bar strain obtained from displacement measurements at the peak resistance and $\varepsilon_{sa} = 1.99\%$ the corresponding strain calculated using model M_M. Model M_MS was then obtained from model M_M by adding $\varepsilon_{s,app}$ to all computed strains. The moment-curvature diagram for model M_MS is plotted in Fig. 11b (green solid triangles), showing a very good agreement with the experimental diagram. The numerical values for the four data points are also summarized in Table 4. It is worth noting that considering the bar slip via apparent strain $\varepsilon_{s,app}$ leads to significant curvature increases, but does not imply modifications of bending resistance with respect to model M_M. In fact, the internal stresses were still evaluated for strains $\varepsilon_{sa} = \varepsilon_{ssa} - \varepsilon_{s,app}$, i.e., the same strain values used to calculate stresses in model M_M. This feature follows from the choice of keeping the neutral axis depth predicted by model M_M unchanged and releasing the planarity assumption for the joint section by calculating curvature through Eq. (22).

For the cyclic load case, an apparent bar strain due to slip is defined in analogy with model M_MS. In particular, model C_MS was obtained from model C_M by simply adding apparent strain

$$\varepsilon_{s,app} = 0.28\% = \varepsilon_{ym} \tag{24}$$

to all computed strains and evaluating curvature from Eq. (22). The corresponding moment-curvature diagram fits very well the envelope of the experimental diagram (green solid circles in Fig. 11b). Even in this case, the numerical values for the four data points of the curve are reported in Table 4.

5.3. Models accounting for the bar slip via a pseudo stress-strain relationship

As an alternative approach, the bar slip can be accounted for by assigning to the grouted bars a pseudo stress-strain relationship (Ameli and Pantelides 2017) characterized by an increased deformability in comparison with typical reinforcing bars. This greater deformability is reproduced starting from the elastic range through the adoption of a reduced elastic modulus. However, using the pseudo stress-strain relationship and enforcing the planarity of the cross-sections alter the stress evaluation, leading to inaccuracies in the representation of bending moments and curvatures. This appears evident (see the inclined dashed line in Fig. 12) observing that the increased bar deformability, when the planarity of the cross-sections is enforced, implies reductions in the neutral axis depth, and then in the stress distribution. For example, for the monotonic load case, a pseudo reinforcing bar with yield strain $\varepsilon_{pya} = f_{ym}/E_{sm} + \varepsilon_{s,app}$, with E_{sm} mean elastic modulus for steel (Table 2) and $\varepsilon_{s,app}$ given by Eq. (23), would be characterized by a fictitious elastic modulus approximately equal to $E_{pa} = E_{sm}/6$ (model M_MP in Table 4, diagram not shown in Fig. 11b for clarity). With such an assumption, concrete compressive strain and neutral axis depth at yielding turn out to be 237% greater and 37% smaller, respectively, than predicted by model M_MS. This leads to bending moment and curvature about 7% and 17% larger, respectively. At the peak flexural resistance, bending moment and curvature result 4% and 36% smaller, respectively, compared with the experimental findings. To increase the predicted curvature a further reduction of the elastic modulus should be adopted, with the drawback of worsening the estimate of the joint section resistance. For example, for $E_{pa} = E_{sm}/10$ the predicted curvature at the peak resistance is only slightly improved (still −33% with respect to the experiment), whereas bending moment becomes

10% smaller than the experimental resistance. It is then concluded that the pseudo reinforcing bar model cannot be used to interpret the results of the monotonic load test, because of the very large slip experienced by the grouted bars.

Conversely, to predict the response of the specimen subjected to cyclic loading, a pseudo reinforcing bar model can be used due to the smaller extent of the bar slip. In particular, in model C_MP (Table 4) the projecting bars in tension was assigned a pseudo stress-strain relationship with $E_{pa} = E_{sm}/2$, leading to bending moments differing less than 6% with respect to those obtained with model C_MS, and a satisfactory approximation of the curvature. The value of the reduced elastic modulus is apparently in line with the findings of Ameli and Pantelides (2017) concerning precast bridge columns with grouted splice sleeve connectors.

5.4. Ductility

Three ductility ratios were obtained from the cyclic test on the grouted duct connection (Table 5).

In particular, curvature ductility of the joint section (first column of Table 5) was obtained as the ratio between experimental ultimate curvature (χ_{ju} = 111.9 ‰/m) and yield curvature computed using model C_MS ($\chi_{jy} = \chi_{ja}$ = 17.1 ‰/m). It appears evident from Table 4 (models C_M and C_MS) that the slip of grouted bars has the effect of reducing significantly the ductility. If conventional yield curvature (Priestley et al. 2007, IMIT 2018)

$$\chi'_{jy} = \chi_{jy} M_{jmax} / M_{jya} \tag{25}$$

is used instead of χ_{jy}, curvature ductility becomes $\mu_{\chi j} = \chi_{ju}/\chi'_{jy}$ = 5.77, with a reduction of 12%. In the previous equation, M_{jmax} = 605 kNm and M_{jya} = 534 kNm are experimental maximum bending moment and yield moment according with model C_MS (Table 4), respectively.

Displacement ductility (second column of Table 5) is the ratio between experimental deflections corresponding to ultimate and yield curvatures and represents a measure of overall ductility of the structural system. This ductility ratio is usually attributed to flexural deformations.

However, it is shown above that displacement Δ contains a certain amount of shear slip at the column-foundation interface. In particular, ultimate displacement (Δ_u = 155.1 mm) contains shear slip s_u = 7.3 mm, whereas at yielding (Δ_y = 34.4 mm) the shear slip is s_y = 1.0 mm. Ratio μ_Δ is only 69% of $\mu_{\chi j}$. This feature, quite usual also for cast-in-place structures, is a consequence of the fact that the critical region of the column is significantly shorter compared with the shear span.

Another overall ductility ratio, not including the effects due to shear slip, can be defined as $\mu_\theta = (\Delta_u - s_u)/(\Delta_y - s_y) = \theta_u/\theta_y$ (third column of Table 5). Due to the relatively small extent of the shear slip occurred during the test, μ_θ is only 2% lower than μ_Δ. A comparison in terms of drift ductility between the present specimen and one of the cast-in-place specimens tested by Popa et al. (2015) is reported in the last column of Table 3. The ductility for specimen CIP2, not explicitly reported in that paper, was deduced from text. Observing the cyclic force-displacement plot presented for that specimen, it seems that in correspondence of the maximum drift reached at the end of test, equal to 5%, a resistance drop of roughly 15% was achieved. Then, consistently with the present paper, the drift of 5% may be identified with θ_u. Moreover, strain gauges measurements presented by Popa et al. (2015) showed that bar yielding was achieved for θ_y = 1%. This justifies ratio μ_θ reported in Table 3. It is worth noting that, in the absence of shear slip measurements, for specimen CIP2 ductility ratios μ_θ and μ_Δ coincide. In conclusion, the grouted duct connection proposed possesses ductility characteristics analogous to those of comparable monolithic connections.

For the tested column, assuming the centroid of the plastic hinge positioned at the column-foundation interface due to strain penetration into the foundation (Megalooikonomou et al. 2018), ultimate and yield deflections, shear slips and curvatures are linked with each other by the following relation:

$$\Delta_u - s_u = \Delta_y - s_y + (\chi_{ju} - \chi_{jy}) l_p L_\Delta , \tag{26}$$

where l_p is the plastic hinge length. This equation represents a modification of an expression, derived by Priestley et al. (2007) and universally used (see for example Belleri and Riva 2012), which neglects the shear slip. Solving Eq. (26) for l_p, length $l_p = 431$ mm is obtained (last column of Table 5). This value, slightly smaller than the cross-section depth, is comparable with that usually attributed to cast-in-place columns (CEB 2004b).

Table 5 Ductility ratios and plastic hinge length obtained from the cyclic test

$\mu_{\chi j} = \chi_{ju}/\chi_{jy}$	$\mu_\Delta = \Delta_u/\Delta_y$	$\mu_\theta = \theta_u/\theta_y$	l_p/H
6.54	4.51	4.42	0.86

5.5. Design moment-curvature diagram

Two additional models, namely C_D and C_DS (Table 4), were used to compute the moment-curvature diagram of the joint section subjected to the cyclic load test. These models adopt design values of material properties. Concrete strength class C40/50 was assumed (see Sect. 3.1). For concrete in compression, a parabola-rectangle relationship according to CEN (2004a) was used, showing strength $f_{cd} = \alpha_{cc} f_{ck}/\gamma_c = 22.7$ MPa (IMIT 2018). After the attainment of the peak flexural resistance and concrete cover removal, increased properties were defined for the concrete core (see the Appendix).

For the longitudinal reinforcing steel, an elastic-perfectly plastic relationship was adopted with $E_s = 200$ GPa, $f_{yd} = 391$ MPa and $\varepsilon_{td} = 6.75\%$ (IMIT 2018).

Model C_D neglects the slip of the projecting bars. The corresponding diagram is reported with black open circles in Fig. 11b.

Model C_DS takes account of the bar slip via an apparent strain. In analogy with model C_MS, apparent strain was assumed to be (see Eq. (24)) $\varepsilon_{s,app} = \varepsilon_{yd} = f_{yd}/E_s = 0.20\%$. The corresponding diagram is reported with green open circles in Fig. 11b. Design moment resistance results to be $M_{ja} = M_{Rd} = 425$ kNm. Thus, the connection system proposed exhibited an over-strength factor of $M_{j,max}/M_{Rd} = 1.41$, very close to the over-strength of 1.35 found by Tullini and Minghini (2016) for

the monotonic test. Design curvature ductility is given by $\mu_{\chi j} = 3.61$. Therefore, the gain in ductility exhibited by the connection system is 6.54/3.61 = 1.81. A generalization of this factor for use in design would need the knowledge of the connection response for various values of N and deserves further investigations.

6. CONCLUSIONS

The connection system investigated, first proposed by Tullini and Minghini (2016), has the steel ducts positioned along the sides of the column cross-section. Therefore, differently from similar connections presented in the literature, in which the ducts are placed at the cross-section corners, this system allows for using traditional reinforcement cages for the column, with longitudinal bars at both mid-side and corners of the cross-section. The length of the lap splice between projecting and regular column bars was designed on the basis of the Eurocode 2 provisions (see Sections 8.4.2, 8.4.3 and 8.7.3 of Eurocode 2, CEN 2004a), neglecting the confinement effect provided by the ducts. The amount of transverse reinforcement along the splice region was defined to meet the requirements reported in Section 8.7.4 of Eurocode 2. For the particular arrangement of 20 mm-diameter longitudinal bars shown in Fig. 1a, the minimum required lap length and the actual lap length resulted to be of 900 mm (45 $\varnothing_b$) and 1 m (50 $\varnothing_b$), respectively. The transverse reinforcement along the splice was comprised of 8 mm-diameter square and diamond-shaped stirrups every 100 mm. Due to the bars positions, the design bending strength of the column far away from the joint section is 4.5% larger than that of the joint section itself.

The experimental programme initiated by Tullini and Minghini (2016) is completed in the present paper with a full-scale test in cyclic bending combined with an axial compression of 1700 kN, resulting in $\nu_d = N/(A_c f_{cd}) = 0.3$. Although the test results for only one precast specimen are presented here, the key response parameter for the connection system are believed to be exhaustively described by gathering together the present findings and results obtained from Tullini and Minghini (2016).

The connection system, used here for a column-to-foundation joint, was subjected to 19 loading cycles achieving a drift of 5.3% in correspondence of a degradation of 15% of the peak resistance. Failure concentrated mainly at the joint section, where yielding and hardening of the projecting bars occurred. The shear slip at the column-foundation interface, activated by plasticization at the column base, led to a slight reduction of second order effects. The maximum measured slip was approximately 5% of the column deflection.

The cyclic bending test presented in this paper was compared, in terms of moment-curvature diagram of the joint section, with one of the monotonic bending tests described by Tullini and Minghini (2016), where substantially the same axial compression was applied. From this comparison, the influence of the loading protocol appears quite significant. In particular, under cyclic loading the connection displayed a strongly smaller deformability. This difference was ascribed to the extent of the slip of the projecting bars within their ducts, which was very smaller in the cyclic load test probably due to the compaction of the injection grout caused by load reversals.

Several analytical models were compared with the aim of interpreting cyclic and monotonic load tests. In particular, it was found that neglecting the bar slip leads to underestimate the curvature also for the cyclic load case. Therefore, it was proposed to take account of the slip by introducing an apparent bar strain. For the cyclic and monotonic load cases, the apparent bar strain to be used to predict accurately the experimental behaviour resulted $\varepsilon_{s,app} = \varepsilon_{ym}$ and $5.4\varepsilon_{ym}$, respectively (models C_MS and M_MS in Table 4 and Fig. 11b). It is worth underlining that these strain values are strictly based on the test results compared in this paper. The amount of the apparent strain due to bar slip varies a lot depending on the loading history, and might be dependent on the detailing of the grouted duct connection. Experiments analogous to those described by Raynor et al. (2002), with a direct measurement of the bar slip, may be used to obtain an appropriate value of the apparent strain to be adopted in calculations. That said, the validity of the proposed method lies in the fact that the use of apparent strains makes the cross-section deformability increase without alter the bending resistance. Conversely, pseudo reinforcing bar models based on a reduced Young's modulus alter

the stress distribution in the cross-section and may lead to inaccurate resistance evaluations. For the proposed connection, assigning to the projecting bars a pseudo stress-strain relationship analogous to that described by Ameli and Pantelides (2017) leads to a satisfactory approximation of the cyclic response and to an inaccurate approximation of the monotonic behaviour (see models C_MP and M_MP in Table 4).

Displacement and curvature ductilities obtained from cyclic test were 4.5 and 6.5, respectively. Compared with model C_DS (Table 4 and Fig. 11b) using design values of material properties, the test showed for the joint section an over-strength factor of 1.4 and a gain in ductility of 1.8. The plastic hinge length deduced from the cyclic test is 86% the cross-section depth.

Dissipated energy and drift ductility were comparable with those reported by Popa et al. (2015) for a cast-in-place specimen pushed up to the same maximum drift and having approximately the same capacity as the specimen described in this paper. Ying and Jin-Xin (2018) showed that column aspect ratio L_{Δ}/H (i.e., shear span length over column cross-section depth) influences failure mode and ductility of RC columns. Therefore, the remarkable ductility shown by the specimen described in this paper should be regarded with care when using the same connection system but with a different aspect ratio.

The design bending strength of the column far away from the joint section (cross-section D-D in Fig. 2b) is only 4.5% larger than that of the joint section itself. This difference is essentially due to the different positions of bars within the relevant cross-sections. The use of projecting bars with a larger diameter compared with that of regular reinforcing bars in the column would result in a greater strength for the joint than for the column. Anyway, the experimental connection strength still is 35% greater than the design strength of the column.

ACKNOWLEDGEMENTS

The present investigation was developed in the framework of the Research Program FAR 2019 of the University of Ferrara. Moreover, the analyses were carried out within the activities of the

(Italian) University Network of Seismic Engineering Laboratories–ReLUIS in the research program funded by the (Italian) National Civil Protection – Progetto Esecutivo 2019/21 – WP2. The test specimen was provided by Prefabbricati Morri srl in Rimini, Italy. A special acknowledgement is due to Dr. Luisfilippo Lanza and Mr. Roberto Mazza for their contribution to the preparation of the experimental test, and to Dr. Massimo Vichi for the video editing.

APPENDIX

This appendix reports the lap splice design (Table 6) and calculation of concrete properties due to confinement (Tables 7 and 8). The confined concrete core characteristics are shown in Fig. 13.

Table 6 Design lap length for the longitudinal column reinforcement and transverse reinforcement requirements along the lap splice (CEN 2004a). The calculations assume concrete strength class C40/50

Symbol	Description [Units]	Equation/Condition/Fig.	Value
f_{ck}	Characteristic compressive strength for concrete [MPa]		40
$f_{ctk,0.05}$	Characteristic tensile strength for concrete [MPa]		2.50
γ_c	Partial safety factor for concrete [-]		1.50
f_{ctd}	Design tensile strength for concrete [MPa]	$f_{ctd} = f_{ctk,0.05}/\gamma_c$	1.67
f_{yk}	Characteristic yield strength for reinforcing steel [MPa]		450
γ_s	Partial safety factor for reinforcing steel [-]		1.15
f_{yd}	Design yield strength for reinforcing steel [MPa]	$f_{yd} = f_{yk}/\gamma_s$	391
$\varnothing_b$	Diameter of longitudinal reinforcement bars [mm]		20
$\varnothing_{st}$	Diameter of transverse reinforcement bars [mm]		8
η_1	Coefficient related to bond conditions and bar position during casting [-]	For poor bond condition	0.7
η_2	Coefficient related to longitudinal bar diameter [-]	For $\varnothing_b \le 32$ mm	1.0
f_{bd}	Design ultimate bond stress for reinforcing bars in concrete [MPa]	$f_{bd} = 2.25\eta_1\eta_2 f_{ctd}$	2.63
$l_{b,rqd}$	Basic required anchorage length [mm]	$l_{b,rqd} = \varnothing_b f_{yd}/4 f_{bd}$	745
c_d	Minimum concrete cover for longitudinal bars [mm]		50
K	Coeff. related with the relative position of longit. and transv. bars [-]	Bar engaged by a stirrup corner (see Fig. 1a)	0.1
A_s	Area of a single spliced bar [mm^2]	$A_s = \pi\varnothing_b^2/4$	314
ΣA_{st}	Area of stirrups per each longit. bar along the anchorage length [mm^2]	$\Sigma A_{st} = 10\,\pi\varnothing_{st}^2/4$	503
$\Sigma A_{st,min}$	Area of the minimum transverse reinforcement [mm^2]	$\Sigma A_{st,min} = A_s$	314
λ	Coefficient related with the area of reinforcement [-]	$\lambda = (\Sigma A_{st} - \Sigma A_{st,min})/A_s$	0.60
ρ_1	Percentage of bars lapped at the column base [%]		100
d_{max}	Maximum clear distance between projecting and regular bars [mm]	See Fig. 1a	82
l_{add}	Additional lap length due to a d_{max} exceeding $4\varnothing_b$ or 50 mm [mm]	$l_{add} = d_{max}$	82
α_1	Coefficient accounting for bar shape [-]	For straight bar	1.00
α_{2t}	Coefficient accounting for concrete cover, bar in tension [-]	$\alpha_{2t} = 1 - 0.15(c_d - \varnothing_b)/\varnothing_b$	0.78
α_{2c}	Coefficient accounting for concrete cover, bar in compression [-]	For all types of anchorage	1.00
α_{3t}	Coefficient accounting for confinement, bar in tension [-]	$\alpha_{3t} = 1 - K\lambda$	0.94
α_{3c}	Coefficient accounting for confinement, bar in compression [-]	For all types of anchorage	1.00
α_5	Coefficient accounting for confinement by transverse pressure p [-]	For $p = 0$	1.00
α_{6t}	Coefficient accounting for the value of ρ_1, bar in tension [-]	For $\rho_1 \ge 50$	1.50
α_{6c}	Coefficient accounting for the value of ρ_1, bar in compression [-]	For all types of anchorage	1.00
l_{0t}	Design lap length in tension [mm]	$l_{0t} = \alpha_1\alpha_{2t}\alpha_{3t}\alpha_5\alpha_{6t} l_{b,rqd} + l_{add}$	897
l_{0c}	Design lap length in compression [mm]	$l_{0c} = \alpha_1\alpha_{2c}\alpha_{3c}\alpha_5\alpha_{6c} l_{b,rqd} + l_{add}$	828
l_0	Actual lap length [mm]	$l_0 \ge \max\{l_{0t}, l_{0c}\}$	1000
$\Sigma A_{st}/2$	Area of stirrups per each longit. bar in tension, to be placed at the outer sections of the lap within $l_0/3$ of the lap length [mm^2]	$\Sigma A_{st}/2 = 4\,\pi\varnothing_{st}^2/4 \ge A_s/2$ (see Fig. 2a)	201

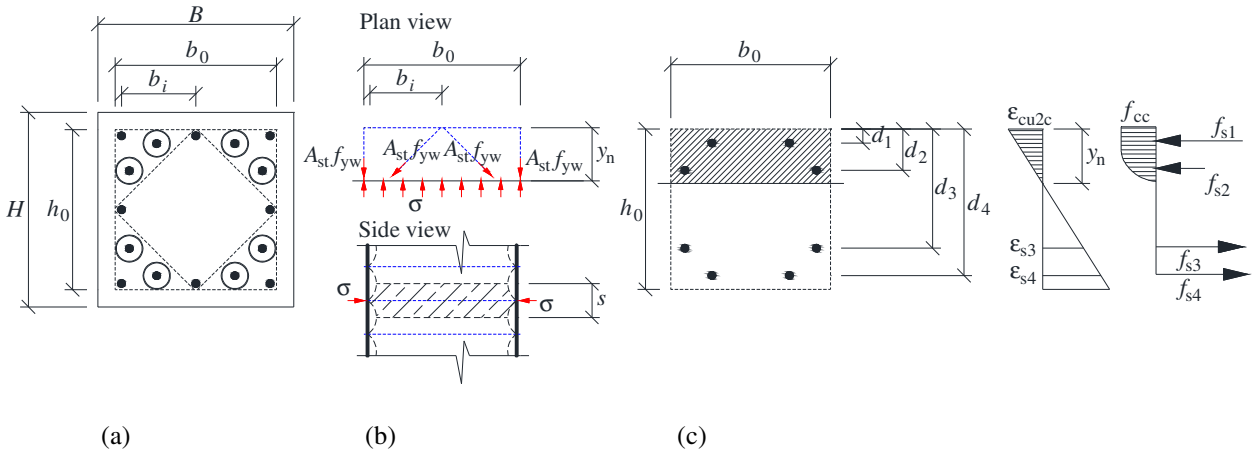

(a) (b) (c)

Fig. 13 Evaluation of the post-peak bending resistance for the joint section: (a) stirrups arrangement and positions of engaged bars; (b) equilibrium condition for the calculation of confining stress σ on the compressed concrete core and (c) effective cross-section with strain and stress diagrams

Table 7 Concrete core geometry and confinement effectiveness factor

Symbol, description [Units]		Equation	Value
$B = H$	Column cross-section dimensions [mm]		500
c	Clear concrete cover [mm]		42
$\varnothing_b$	Diameter of longitudinal reinforcement bars [mm]		20
$\varnothing_{st}$	Diameter of transverse reinforcement bars [mm]		8
n	No. of engaged bars (= No. of projecting bars) [mm]		8
s	Spacing of transverse reinforcement [mm]		100
d_{i0}	Distance of the i-th layer of projecting bars from the top [mm] Joint section in Fig. 2b (i = 1, ..., 4)		80; 150; 350; 420
A_s	Cross-sectional area of one longitudinal bar [mm^2]	$A_s = \pi\varnothing_b^2/4$	314
A_{st}	Cross-sectional area of one leg of transverse reinforcement [mm^2]	$A_{st} = \pi\varnothing_{st}^2/4$	50
$b_0 = h_0$	Dimensions of confined core (to the centreline of the stirrups) [mm]	$b_0 = B - 2c - \varnothing_{st}$	408
b_i	Distance between consecutive engaged bars [mm]	$b_i = 1/2\left(b_0 - \varnothing_{st} - \varnothing_b\right)$	190
d_i	Distance of the i-th layer of projecting bars from the top [mm] Joint section in Fig. 13c (i = 1, ..., 4)	$d_i = d_{i0} - c - \varnothing_{st}/2$	34; 104; 304; 374
α_n	Confinement factor, see CEB (1998) and CEN (2004b) [-]	$\alpha_n = 1 - \sum_{i=1}^{n} b_i^2/6b_0^2$	0.71
α_s	Confinement factor, see CEB (1998) and CEN (2004b) [-]	$\alpha_s = \left(1 - s/2b_0\right)^2$	0.77
α	Confinement effectiveness factor [-]	$\alpha = \alpha_n\alpha_s$	0.55

Table 8 Computed properties for confined concrete. Subscripts 'm', 'k' and 'd' stand for mean, characteristic and design property, respectively

Symbol, description [Units]		Equation	Value		
			$(\cdot)_m$	$(\cdot)_k$	$(\cdot)_d$
f_c	Unconfined concrete compressive strength [MPa]		50.9	40.0	22.7
f_{yw}	Yield strength of transverse reinforcement [MPa]		518	450	391
σ	Confining stress, see CEB (1998) [MPa]	$\sigma = \alpha A_{st} f_{yw}\left(2+\sqrt{2}\right)\Big/ sb_0$	1.19	1.04	0.90
f_{cc}	Compressive strength for confined concrete, see CEB (2004a) [MPa]	$f_{cc} = f_c\left(1+5\sigma/f_c\right)$	56.8	45.2	25.6[a]
$\lvert\varepsilon_{c2c}\rvert$	Compressive strain at the attainment of peak strength for confined concrete, see CEB (2004a) [‰]	$\varepsilon_{c2c} = \varepsilon_{c2}\left(f_{cc}/f_c\right)^2$	2.50	2.55	
$\lvert\varepsilon_{cu2c}\rvert$	Ultimate compressive strain for confined concrete, see CEB (2004a) [‰]	$\varepsilon_{cu2c} = \varepsilon_{cu2} + 0.2\sigma/f_c$	9.88[b]	8.68[c]	
y_n	Neutral axis depth [mm]	y_n from section analysis	100.0		180.4
f_{si}	Stress in projecting bars [MPa]	f_{si} from section analysis	–560;		–391;
	Joint section in Fig. 13c (i = 1, ..., 4)		79;		–391;
			574;		391;
			581		391
χ_{ju}	Ultimate curvature (see Table 4, model C_M) [‰/m]	$\chi_{ju} = \varepsilon_{cu2c}/y_n$	98.8		48.1

Notes:

[a] Evaluated from $f_{ccd} = \alpha_{cc} f_{cck}/\gamma_c$ = 25.6 MPa, where α_{cc} = 0.85 and γ_c = 1.5;

[b] Evaluated for $\lvert\varepsilon_{cu2c}\rvert$ = 5.19‰, i.e., the maximum concrete strain recorded in the test before spalling;

[c] Evaluated for $\sigma = \sigma_k$ = 1.04 MPa, $f_c = f_{ck}$ = 40.0 MPa and $\lvert\varepsilon_{cu2c}\rvert$ = 3.5‰.

REFERENCES

ACI (American Concrete Institute) (2013) ACI 374 – Guide for testing reinforced concrete structural elements under slowly applied simulated seismic loads, Farmington Hills, MI

Ameli MJ, Brown DN, Parks JE, Pantelides CP (2016) Seismic column-to-footing connections using grouted splice sleeves. ACI Structural Journal 113(5):1021-1030

Ameli MJ, Pantelides CP (2017) Seismic analysis of precast concrete bridge columns connected with grouted splice sleeve connectors. Journal of Structural Engineering 143(2):04016176

Belleri A, Brunesi E, Nascimbene R, Pagani M, Riva P (2015) Seismic performance of precast industrial facilities following major earthquakes in the Italian territory. Journal of Performance of Constructed Facilities 29(5):04014135

Belleri A, Riva P (2012) Seismic performance and retrofit of precast concrete grouted sleeve connections. PCI Journal 57(1):97-109

Bovo M, Savoia M (2018) Numerical simulation of seismic-induced failure of a precast structure during the Emilia earthquake. Journal of Performance of Constructed Facilities 32(1):04017119

Bruggeling ASG, Huyghe GF (1991) Prefabrication with Concrete. A. A. Balkema, Rotterdam

Buratti N, Bacci L, Mazzotti C (2014) Seismic behaviour of grouted sleeve connections between foundations and precast columns. In: Proceedings of the 2nd European Conference on Earthquake Engineering and Seismology. Istanbul, August 25-29

Buratti N, Minghini F, Ongaretto E, Savoia M, Tullini N (2017) Empirical seismic fragility for the precast RC industrial buildings damaged by the 2012 Emilia (Italy) earthquakes. Earthquake Engineering and Structural Dynamics 46(14):2317-2335

CEB (Euro-International Committee for Structural Concrete) (1998) CEB-FIP Model Code 1990 - Design Code, 2nd edn. Thomas Telford, London

CEN (European Committee for Standardization) (2004a) EN 1992-1-1:2004, Eurocode 2 – Design of concrete structures – Part 1-1: General rules and rules for buildings. CEN, Brussels

CEN (European Committee for Standardization) (2004b) EN 1998-1:2004, Eurocode 8 – Design of structures for earthquake resistance – Part 1: General rules, seismic actions and rules for buildings. CEN, Brussels

Dal Lago B, Toniolo G, Lamperti Tornaghi M (2016) Influence of different mechanical column-foundation connection devices on the seismic behaviour of precast structures. Bulletin of Earthquake Engineering 14(12):3485-3508

Demartino C, Vanzi I, Monti G, Sulpizio C (2018) Precast industrial buildings in Southern Europe: loss of support at frictional beam-to-column connections under seismic actions. Bulletin of Earthquake Engineering 16(1):259-294

Elliott KS (2017) Precast Concrete Structures, 2nd edn. CRC Press, Taylor & Francis Group, Boca Raton

FEMA (Federal Management Emergency Agency) (2000) FEMA 356 – Prestandard and commentary for the seismic rehabilitation of buildings. Washington, D.C.

FIB (International Federation for Structural Concrete) (2003) Seismic design of precast concrete building structures, Bulletin No. 27, ISBN 978-2-88394-067-3

FIB (International Federation for Structural Concrete) (2016) Precast-concrete buildings in seismic areas, Bulletin No. 78, ISBN 978-2-88394-118-2

Hua LJ, Rahman ABA, Ibrahim IS (2014) Feasibility study of grouted splice connector under tensile load. Construction and Building Materials 50:530-539

IMIT (Italian Ministry of Infrastructure and Transport) (2018) Italian Building Code-D.M. 17/01/2018, Rome [in Italian]

Kuttab AS, Dougill JW (1988) Grouted and dowelled jointed precast concrete columns - Behaviour in combined bending and compression. Magazine of Concrete Research 40(144):131-142

Liu Y, Zhou B, Cai J, Sang-Hoon Lee D, Deng X, Feng J (2018) Experimental study on seismic behavior of precast concrete column with grouted sleeve connections considering ratios of longitudinal reinforcement and stirrups. Bulletin of Earthquake Engineering, https://doi.org/10.1007/s10518-018-0414-9

Megalooikonomou KG, Tastani SP, Pantazopoulou SJ (2018) Effect of yield penetration on column plastic hinge length. Engineering Structures 156:161-174

Minghini F, Ongaretto E, Ligabue V, Savoia M, Tullini N (2016) Observational failure analysis of precast buildings after the 2012 Emilia earthquakes. Earthquakes and Structures 11(2):327-346

Negro P, Toniolo G (eds.) (2012) Design guidelines for connections of precast structures under seismic actions. EUR - Scientific and Technical Research Reports. JRC Publication No. JRC71599. Publications Office of the European Union, http://dx.doi.org/10.2777/37605

NI (National Instruments) (2015) LabVIEW 2015 Help. Available at http://www.ni.com/support. Accessed 23 February 2015

Park R (1988) Ductility evaluation from laboratory and analytical testing (State-of-the-Art Report). In: Proceedings of the 9th World Conference on Earthquake Engineering. Tokyo-Kyoto, August 2-9

Park R (1995) Perspective on the Seismic Design of Precast Concrete Structures in New Zealand. PCI Journal 40(3):40-60

PEER (Pacific Earthquake Engineering Research Center) (2004) Structural Performance Database User's manual, University of Berkeley. Available at https://nisee.berkeley.edu/spd/. Accessed 1 July 2018

Popa V, Papurcu A, Cotofana D, Pascu R (2015) Experimental testing on emulative connections for precast columns using grouted corrugated steel sleeves. Bulletin of Earthquake Engineering 13(8):2429-2447

Priestley MJN, Calvi GM, Kowalsky MJ (2007) Displacement-based seismic design of structures. Pavia IUSS Press, Pavia

Rave-Arango JF, Blandón CA, Restrepo JI, Carmona F (2018) Seismic performance of precast concrete column-to-column lap-splice connections. Engineering Structures 172:687-699

Raynor DJ, Lehman DE, Stanton JF (2002) Bond-slip response of reinforcing bars grouted in ducts. ACI Structural Journal 99(5):568-576

Savoia M, Buratti N, Vincenzi L (2017) Damages and collapses in industrial precast buildings after the 2012 Emilia earthquake. Engineering Structures 137:162-180

Sezen H, Whittaker AS (2006) Seismic performance of industrial facilities affected by the 1999 Turkey earthquake. Journal of Performance of Constructed Facilities 20(1):28-36

Toniolo G, Colombo A (2012) Precast concrete structures: The lessons learned from L'Aquila earthquake. Structural Concrete 13(2):73-83

Tullini N, Minghini F (2016) Grouted sleeve connections used in precast reinforced concrete construction - Experimental investigation of a column-to-column joint. Engineering Structures 127:784-803

Verderame GM, Fabbrocino G, Manfredi G (2008a) Seismic response of r.c. columns with smooth reinforcement. Part I: Monotonic tests. Engineering Structures 30(9):2277-2288

Verderame GM, Fabbrocino G, Manfredi G (2008b) Seismic response of r.c. columns with smooth reinforcement. Part II: Cyclic tests. Engineering Structures 30(9):2289-2300

Yan Q, Chen T, Xie Z (2018) Seismic experimental study on a precast concrete beam-column connection with grout sleeves. Engineering Structures 155:330-344

Yanev P (1989) Performance of industrial facilities. Earthquake Spectra 5(3):101-113

Yuan H, Zhenggeng Z, Naito CJ, Weijian Y (2017). Tensile behavior of half grouted sleeve connections: Experimental study and analytical modeling. Construction and Building Materials 152:96-104

Ying M, Jin-Xin G (2018) Seismic failure modes and deformation capacity of reinforced concrete columns under cyclic loads. Periodica Polytechnica Civil Engineering 62(1):80-91

Zheng LX (1996) Grouted precast concrete column connections under reversed cyclic bending and compression. ACI Structural Journal 93(3):247-256